



**HAL**  
open science

# High-pressure serpentization and abiotic methane formation in metaperidotite from the Appalachian subduction, northern Vermont

Antoine Boutier, Alberto Vitale Brovarone, Isabelle Martinez, Olivier Sissmann, Sara Mana

## ► To cite this version:

Antoine Boutier, Alberto Vitale Brovarone, Isabelle Martinez, Olivier Sissmann, Sara Mana. High-pressure serpentization and abiotic methane formation in metaperidotite from the Appalachian subduction, northern Vermont. *Lithos*, 2021, 396-397, pp.106190. 10.1016/j.lithos.2021.106190 . hal-03388726

HAL Id: hal-03388726

<https://ifp.hal.science/hal-03388726>

Submitted on 9 May 2023

**HAL** is a multi-disciplinary open access archive for the deposit and dissemination of scientific research documents, whether they are published or not. The documents may come from teaching and research institutions in France or abroad, or from public or private research centers.

L'archive ouverte pluridisciplinaire **HAL**, est destinée au dépôt et à la diffusion de documents scientifiques de niveau recherche, publiés ou non, émanant des établissements d'enseignement et de recherche français ou étrangers, des laboratoires publics ou privés.



Distributed under a Creative Commons Attribution - NonCommercial 4.0 International License

1 **High-pressure serpentinization and abiotic methane formation in metaperidotite from the**  
2 **Appalachian subduction, northern Vermont**

3 Antoine Boutier<sup>1,2\*</sup>, Alberto Vitale Brovarone<sup>3,4\*</sup>, Isabelle Martinez<sup>2</sup>, Olivier Sissmann<sup>5</sup>, Sara  
4 Mana<sup>6</sup>

5 <sup>1</sup>*Dipartimento di Scienze della Terra, Università degli Studi di Torino, Via Valperga Caluso 35,*  
6 *Torino, Italy*

7 <sup>2</sup>*Université de Paris, Institut de physique du globe de Paris, CNRS, F-75005 Paris, France*

8 <sup>3</sup>*Dipartimento di Scienze Biologiche, Geologiche e Ambientali, Alma Mater Studiorum*  
9 *Università di Bologna. Piazza di Porta San Donato 1, Bologna, Italy*

10 <sup>4</sup>*Institut de Minéralogie, de Physique des Matériaux et de Cosmochimie (IMPMC), Sorbonne*  
11 *Université, Muséum National d'Histoire Naturelle, UMR CNRS 7590, IRD UR206, 75005 Paris,*  
12 *France*

13 <sup>5</sup>*IFP Energies Nouvelles, 92500 Rueil-Malmaison, France*

14 <sup>6</sup>*Department of Geological Sciences, Salem State University, Salem, MA 01970, USA*

15 \*Corresponding author: [antoine.boutier@unito.it](mailto:antoine.boutier@unito.it), [alberto.vitaleb@unibo.it](mailto:alberto.vitaleb@unibo.it)

## 1 Introduction

2 Alteration of ultramafic rocks by aqueous fluids, or serpentinization, produces serpentine-  
3 rich rocks and may be accompanied by redox reactions leading to the formation of H<sub>2</sub> and  
4 abiotic light hydrocarbons (Mével, 2003; Moody, 1976; Seyfried et al., 2007). Oxidation of  
5 Fe<sup>2+</sup> in mantle minerals and formation of Fe<sup>3+</sup> minerals such as magnetite produces H<sub>2</sub>,  
6 which may then promote the conversions of dissolved carbon-bearing species into abiotic  
7 CH<sub>4</sub> (Andréani et al., 2013; Berndt et al., 1996). Serpentinization is well documented at mid-  
8 ocean ridges and on land (Andréani et al., 2007; Cannat et al., 2010; Etiope et al., 2011; Klein  
9 et al., 2014; Schrenk et al., 2013), where H<sub>2</sub> and CH<sub>4</sub> produced through serpentinization can  
10 support biological communities and could be linked to the emergence of early life on Earth  
11 (Kelley et al., 2005; Ménez et al., 2018; Sleep and Bird, 2007). Serpentinization processes  
12 may also happen at much greater depths and affect subducted mantle sections and the  
13 overlying mantle wedge at convergent margins (Guillot et al., 2015, 2000; Vitale Brovarone  
14 et al., 2017; Wada et al., 2008), owing to the availability of aqueous fluids (Bebout and  
15 Penniston-Dorland, 2016; Deschamps et al., 2013). However, the patterns of  
16 serpentinization reactions at high-temperature (HT) and high-pressure (HP) conditions, here  
17 defined with respect to the serpentine stability field, and the associated fluid-rock redox  
18 budgets are still largely unconstrained. The possibility that HT-HP serpentinization may not  
19 involve Fe oxidation and genesis of H<sub>2</sub> at 400-600°C has been proposed (Evans, 2010).  
20 However, natural case studies of slab and mantle wedge-derived serpentinized peridotites  
21 suggest that magnetite, H<sub>2</sub> and abiotic CH<sub>4</sub> can be produced at these conditions (Vitale  
22 Brovarone et al., 2020). Ultramafic bodies in metamorphic belts can provide insights on the  
23 mechanisms of HP-HT serpentinization and the resulting fluids (Evans et al., 2017), and

24 therefore make good case studies for the investigation of the mechanisms of  
25 serpentinization in subduction zones.

26 The Belvidere ultramafic complex, Vermont, USA, is a fragment of the former Iapetus ocean  
27 that was involved in the Taconic orogeny and recorded subduction-related HP  
28 metamorphism during Cambrian-Ordovician (Chew and van Staal, 2014; Gale, 1980;  
29 Honsberger et al., 2017). This complex includes variably serpentinized peridotites containing  
30 antigorite, the HT serpentine minerals stable at subduction zone HP conditions (e.g., Evans,  
31 2004; Schwartz et al., 2013), therefore making a potential example of HT-HP  
32 serpentinization. In this work, we integrate field, microstructural, thermodynamic, and fluid  
33 inclusions data to investigate the patterns and timing of serpentinization of the Belvidere  
34 ultramafic complex, with particular focus on the HP fluid-rock interactions recorded by  
35 these rocks.

## 36 **1. Geologic setting**

37 The Belvidere Mountain complex (BMC) area is part of a North-South trending belt of  
38 mafic/ultramafic rocks belonging to the Appalachian Mountain system and extending from  
39 Newfoundland to Georgia (Gale, 2007; Hibbard et al., 2006)(Fig. 1). These ultramafic bodies  
40 mainly consist of variably serpentinized peridotites, and associated metabasic and  
41 metafelsic rocks tectonically embedded within Cambrian-Ordovician metasedimentary and  
42 metavolcanic formations (Chidester et al., 1978; Gale, 1986, 1980; Laird et al., 1984; Van  
43 Baalen et al., 2009). The BMC, as well as other mafic/ultramafic complexes such as the  
44 Tillotson Peak and the Pennington complexes, may represent remnants of an ocean-  
45 continent transition zone associated with the extension of the Laurentian margin (Chew and

46 van Staal, 2014). These terranes were successively involved in the closure of the Iapetus  
47 Ocean during the Ordovician Taconic orogeny (Doolan et al., 1982; Honsberger et al., 2017;  
48 Karabinos et al., 1998; Laird et al., 1984; Stanley et al., 1984). The BMC forms a 6.5 km long  
49 body that structurally overlies the metasedimentary Ottawaquechee and Stowe Formations  
50 to the East and is overlain by the Hazen Notch formation to the West. The Stowe Formation  
51 is late Cambrian, composed of gray-green quartz-chlorite-sericite +/- magnetite schists. The  
52 Ottawaquechee Formation consists of middle Cambrian carbonaceous pyritiferous phyllites.  
53 The Neoproterozoic to Cambrian Hazen Notch Formation includes graphitic and non-  
54 graphitic quartz-albite-sclerite-chlorite schist, along with medium-grained, massive, quartz-  
55 albite-muscovite gneiss. The internal architecture of the BMC comprises, from top to  
56 bottom, variably serpentinized dunite and harzburgite, coarse-grained and fine-grained  
57 amphibolite, greenstone, muscovite schist, and albite gneiss (Gale, 1986, 1980; Van Baalen  
58 et al., 2009). Lenticular bodies composed of talc-carbonate rocks and steatite, often  
59 including cores of relatively un-serpentinized peridotite, are observed within the BMC, and  
60 range in size from a few meters to several tens of meters (Chidester et al., 1978). The BMC  
61 rocks underwent Taconic blueschist-facies peak metamorphic conditions constrained at 0.9-  
62 1.3 GPa and 510-520 °C in metabasic rocks (Honsberger, 2015; Laird et al., 1993). Higher P  
63 metamorphic conditions, up to coesite ultra high-pressure (UHP) conditions, are recorded  
64 by the Tillotson Peak mafic rocks located just north of the BMC (Gonzalez et al., 2020; Laird  
65 et al., 1993, 1984). In the BMC, the HP tectonometamorphic event has been dated at 505-  
66 473 Ma by  $^{40/39}\text{Ar}$  amphibole and mica geochronology (Castonguay et al., 2012; Laird et al.,  
67 1993).

## 68 **2. Methods**

69 Quantitative energy-dispersive X-ray spectroscopy (EDS) analyses and backscattered  
70 electron (BSE) imaging were carried out using the JSM-IT300LV Scanning Electron  
71 Microscope Oxford Inca Energy Dispersive Spectrometer at the Department of Earth  
72 Sciences of Turin University. Data were processed with the INCA software from Oxford  
73 Instruments. Quantitative analysis employed 15kV accelerating voltage and a beam current  
74 of 50 nA and 20 s to 40 s counting total time. Natural and synthetic mineral and oxide  
75 standards were employed. EDS calibration was made using Cobalt standard.

76 Quantitative wavelength-dispersive spectrometer (WDS) analyses were carried out using a  
77 JEOL 8200 Super Probe at the Department of Earth Sciences "Ardito Desio" of Milan  
78 University. The microprobe was using a 15kV accelerating voltage under 5 nA, with 30s  
79 counting time under maximum emission peak. Sixteen oxide composition were measured,  
80 using synthetic and natural standards: grossular (Si, Al and Ca), omphacite (Na), K-feldspar  
81 (K), fayalite (Fe), forsterite (Mg), rhodonites (Mn), niccolite (Ni), ilmenite (Ti), galena (Pb and  
82 S), pure Cr, pure Zn and pure Cu.

83 MicroRaman spectroscopy of minerals and fluid inclusions was done at the Department of  
84 Earth Sciences, University of Turin, with a LabRAM HR (VIS) (HORIBA Jobin Yvon) equipped  
85 with a 532.11 nm, solid-state Nd laser, a Super Notch Plus filter with spectral resolution of 1  
86  $\text{cm}^{-1}$ , and a grating of 600 grooves/mm. The laser of emission power was set at 80 mW and  
87 focused to 5  $\mu\text{m}$  with a 100x objective with a laser power on the sample < 5 mW. Calibration  
88 was performed using the 520.6  $\text{cm}^{-1}$  band of a silicon standard for the 100-2000  $\text{cm}^{-1}$  range,  
89 and the 2331  $\text{cm}^{-1}$  band of atmospheric  $\text{N}_2$  for the 2000-4000  $\text{cm}^{-1}$  range. Four  
90 accumulations of 30–60 s were collected for each spectrum. Raman spectra of fluid  
91 inclusions were performed on double-polished thick sections unless otherwise specified.

92 Isotopic composition measurements of methane were performed on a MAT 253 (Thermo  
93 Fisher) mass spectrometer, coupled with gas chromatography (GCC-IRMS) device as CO<sub>2</sub>  
94 gas, at a specific retention time, on masses 44 (for  $\delta^{12}\text{C}$ ), 45 (for  $\delta^{13}\text{C}$ ) and 46 (for  $\delta^{18}\text{O}$ ),  
95 after the methane is completely oxidized into CO<sub>2</sub> through combustion at 1000°C. This is  
96 because it is not possible to directly measure methane isotopologues ( $^{12}\text{CH}_4$ ,  $^{13}\text{CH}_4$ ,  $^{12}\text{CH}_3\text{D}$ )  
97 on a “classical” magnetic sector IRMS, due to interferences on masses 16, 17 and 18 in the  
98 source (such as CH<sub>5</sub><sup>+</sup>, H<sub>2</sub>O ...). The value of the CO<sub>2</sub> internal reference gas was determined  
99 using multiple IAEA carbonate standards (IAEA-603, 610, 611, 612) on an EA-IRMS device.  
100 On the GCC-IRMS, the efficiency of CH<sub>4</sub> oxidation into CO<sub>2</sub> is checked before each analytical  
101 session by injecting, as a sample, two different commercial external methane isotopic  
102 standard (such as Air Liquide Thermo 1.2 and Air Liquide Bio 1.0 gases). If the analytical  
103 value of the commercial standards is within 0.1‰ of their independently determined value,  
104 then the combustion process is deemed valid and without fractionation. The samples  
105 collected from fluid inclusions can then be analyzed. The gas phase was extracted and  
106 measured after crushing 20 to 30 gr of rock sample under vacuum.

107 Thermodynamic modelling was performed using the Deep Earth Water (DEW) Model  
108 (Huang et al., 2019; Sverjensky et al., 2014) and the EQ3/EQ6 software (Wolery and Jarek,  
109 2003) with a modified Berman database (Berman, 1988). The speciation-solubility code EQ3  
110 was used to calculate the composition of a fluid in equilibrium with a given mineral  
111 assemblage at fixed  $f\text{O}_2$ , P and T, and in the K-Na-Ca-Mg-Fe-Al-Si-O-H-C-N-S-Cl system. The  
112 reaction path modeling code EQ6 was used to model the irreversible reaction between 1kg  
113 of fluid as derived from EQ3 (see section 3.5 for details on different buffering assemblages),  
114 and a given number of moles of minerals constituting a rock reservoir and determining an

115 initial fluid/rock (F/R) ratio for each calculation. The chosen EQ6 mineral assemblage  
116 corresponds to a dunite with mineral modal proportions comparable with the most  
117 preserved study samples and consisting of 92% olivine (forsterite 90%, fayalite 10%), 5.4%  
118 orthopyroxene (enstatite 90%, ferrosilite 10%), 2.5% clinopyroxene (diopside 90%,  
119 hedenbergite 10%) and 0.1% spinel. Additional details regarding the modeling strategy are  
120 presented in Section 3.5.

### 121 **3. Sample description and mineral chemistry**

122 In this section, we present the petrography, microstructures and mineral chemistry of  
123 samples collected in the BMC (Fig. 2). The selected samples range from weakly  
124 serpentinized dunite (V18-2a and V18-2b) to partially serpentinized dunite including layers  
125 of boudinaged meta-pyroxenite (V18-3a and V18-3b), to fully serpentinized peridotite (V18-  
126 B3). One sample of rodingites consisting of carbonates, garnet, epidote and chlorite is also  
127 presented.

#### 128 ***Microstructural characterization***

129 Sample V18-2a (least serpentinized dunite) consists of olivine (~80 vol.%), antigorite (~10  
130 vol.%), Cr-spinel (>5 vol.%), magnetite (<5 vol.%), chlorite (<1 vol.%), sulphides (<1 vol.%),  
131 and alloys (<1 vol.%) determined from visual estimate in thin section. Primary olivine forms  
132 crystals ranging in size from 0.25 to 1 mm (Fig. 3A) partially replaced by antigorite, as  
133 identified by MicroRaman spectroscopy (Fig. 4), along fractures (Fig. 3A-C). Antigorite is  
134 present as elongated crystals, up to 200  $\mu\text{m}$  in length, which statically overgrew the olivine  
135 (Fig. 3C). Magnetite is present in three microstructural domains: as large, millimeter scale

136 crystals rimming chromite relicts, as grains of  $\sim 50 \mu\text{m}$ , and as millimeter scale crystals in  
137 antigorite veins. Chlorite is found, together with magnetite, around Cr-spinel relicts (Fig. 3B).

138 Sample V18-2b (serpentinized dunite) consists of antigorite ( $\sim 40 \text{ vol.}\%$ ), olivine ( $\sim 40 \text{ vol.}\%$ ,  
139 including primary and metamorphic olivine), magnetite ( $>5 \text{ vol.}\%$ ), chlorite ( $>5 \text{ vol.}\%$ ),  
140 brucite ( $<5 \text{ vol.}\%$ ), and alloys ( $<1 \text{ vol.}\%$ ). The structure is similar to V18-2a, but in this case  
141 the extent of serpentinization is higher. SEM backscattered-electron imaging reveals the  
142 presence of a second generation of olivine, hereafter metamorphic olivine (see Section 4.2  
143 for discussion) growing in two different sites: epitaxially on the primary olivine and replacing  
144 former orthopyroxene (Fig. 5A-B). Striped zoning is observed in primary olivine (Fig. 5A), as  
145 described in Plümer et al., 2012a, alternating thin forsterite-richer and forsterite-poorer  
146 olivine composition. The initial presence of orthopyroxene in the rock is inferred based on  
147 the presence of clinopyroxene exsolutions preserved in metamorphic olivine-rich  
148 pseudomorphs (Fig. 3D and 5B). Antigorite is present as elongated (0.5 mm in length)  
149 crystals and as fine-grained aggregates in the matrix. The elongated antigorite crystals are  
150 chemically zoned, with bright core and dark rim in backscattered electron imaging (Fig. 5A).  
151 Raman spectra of both generations exhibit the characteristic  $1043 \text{ cm}^{-1}$  band of antigorite,  
152 whereas the main OH stretching is at  $3664 \text{ cm}^{-1}$  in the bright core and at  $3673 \text{ cm}^{-1}$  in the  
153 dark rim (Fig. 4C), both consistent with antigorite Raman features. The higher Raman shift of  
154 the dark rim may be linked to variation of pressure condition (Auzende et al., 2004). The  
155 dark antigorite generation appears the same forming the fine-grained aggregates. Only the  
156 dark generation was observed in contact with primary and metamorphic olivine (Fig. 5A).  
157 Magnetite is more abundant relative to sample V18-2a. Brucite was identified by SEM  
158 EPMA, and Raman (Fig. 4B) in veins, sometimes associated to metamorphic olivine (Fig. 5C).

159 Alloys and sulphides are present in association with antigorite and are locally associated to  
160 magnetite (Fig. 5D).

161 Samples V18-3a and 3b are from a boudinaged layer of clinopyroxenite included in an  
162 intensely serpentinized dunite (Fig. 3E-G). The mineral assemblage and microstructures of  
163 the serpentinized dunite part of the sample is similar to sample V18-2b, yet more intensely  
164 serpentinized. The primary clinopyroxene is fully replaced by diopside aggregates in both  
165 the clinopyroxenite layer and the host dunite. The primary clinopyroxene sites in this sample  
166 are slightly different from the serpentinized dunite, with less abundant magnetite and  
167 characteristic fan-shaped diopside aggregates in the former compared to the latter.  
168 Metamorphic olivine is present at the rim of primary clinopyroxene and along its cleavages,  
169 together with antigorite (Fig. 5E-F). In the latter case, metamorphic olivine is localized along  
170 thin arrays encircled by antigorite (Fig. 5F). Antigorite shows the same chemical zoning as  
171 observed in the dunite, with brighter cores and darker rims in backscatter electron imaging  
172 (Fig. 5G). Backscattered electron imaging reveals that the dark antigorite shows similar  
173 overgrowth microstructural relationships with both primary and metamorphic olivine (Fig.  
174 5E). The microstructures reflect either equilibrium between antigorite and the two olivine  
175 generations, or overgrowth of both olivine generations by the antigorite. Considering that  
176 the amount of primary olivine strongly decreases in favour of antigorite in several samples,  
177 which suggests serpentinization of the primary olivine, it is suggested that the dark  
178 antigorite generation formed after the growth of metamorphic olivine. It is possible, even  
179 though the microstructures could not confirm it, that the first antigorite generation grew  
180 prior to or together with the metamorphic olivine. Magnetite is present in four different  
181 structural sites: as arrays of  $\sim 50 \mu\text{m}$  size crystals scattered in the rock, as trails of  $\sim 50 \mu\text{m}$

182 crystals in primary olivine and clinopyroxene pseudomorphoses, as aggregates rimming the  
183 primary Cr-spinel, and as millimeter scale aggregates along discordant veins. The Cr-spinel  
184 sites are characterized by three different layers: a rather preserved core, a mantle of  
185 ferritchromite, and a rim of magnetite (Fig. 5E; see Section 4.2).

186 Sample V18-B3 is a fully serpentinized peridotite. The matrix is composed of a mixture of  
187 antigorite and chrysotile (identified by MicroRaman) with magnetite. Brucite is observed  
188 replacing pyroxene sites and is associated with magnetite and/or metamorphic olivine (Fig.  
189 3H and 5H). Based on the microstructural observations on sample V18-2b, these  
190 pseudomorphoses are interpreted as former orthopyroxene crystals replaced by  
191 metamorphic olivine and successively hydrated to form serpentine + brucite ± magnetite.

### 192 **3.1. Mineral chemistry**

193 Primary olivine has Mg# of 0.91-0.92 [ $Mg\# = Mg/(Fe+Mg)$ ], whereas metamorphic olivine is  
194 enriched in Mg (Mg# of 0.95) (Table 1, Fig. 6). The Mn# [ $Mn\# = Mn/(Mn+Fe+Ni)$ ] of  
195 metamorphic olivine ( $0.0040 \pm 0.0006$ ) is much higher than primary olivine ( $0.0015 \pm 0.0005$ ).  
196 Metamorphic olivine analyses in sample V18-B3 show slightly lower Mg# and higher Mn#  
197 content relative to metamorphic olivine from other samples. Metamorphic olivine rimming  
198 the primary orthopyroxene sites in sample V18-3a has higher CaO content (0.25 wt.%)  
199 compared to the metamorphic olivine overgrowing primary olivine in V18-2b (0.02 wt.%).  
200 The NiO content of primary olivine (0.38 to 0.49 wt.%) and metamorphic olivine (0.39 to  
201 0.46 wt.%) are similar.

202 The incorporation of Mn in olivine appears to be characteristic of metamorphic olivine from  
203 several localities worldwide regardless of the olivine formation conditions (dehydration vs.

204 hydration) (Fig. 6) (e.g., Frost and Beard, 2007; Majumdar et al., 2016; Nozaka, 2018, 2003).  
205 The Mg# of metamorphic olivine relative to primary olivine may depend upon several  
206 parameters such as the stability of different Fe-bearing minerals, the Fe partitioning among  
207 them, and P-T and redox conditions. An increase in Mg# (and MnO) in metamorphic olivine  
208 relative to primary olivine has been observed in inferred mantle wedge peridotites  
209 recording HP serpentinization (Dandar et al., 2019; Guillot et al., 2000). Our data, together  
210 with previous work, indicate that iron was not preferentially partitioned into olivine during  
211 HT serpentinization (Evans, 2010) but other Fe-bearing minerals, such as serpentine and  
212 magnetite, could form. Plümper et al., 2012a report striped Mg# zoning similar to the BMC  
213 samples in hydrated supra-subduction mantle rocks as the result of chemical interaction  
214 during antigorite serpentinization at high temperature conditions. Metamorphic olivine  
215 formed through prograde antigorite + brucite dehydration shows either lower or higher  
216 Mg# compared to mantle olivine (Arai et al., 2012; Debret et al., 2013; Iyer et al., 2008;  
217 Kempf and Hermann, 2018; Nozaka, 2018; Plümper et al., 2012b; Scambelluri et al., 1995;  
218 Shen et al., 2015)(Fig. 6).

219 In samples V18-2b and V18-3a, the core of individual, elongated antigorite crystals exhibits  
220 higher FeO (1.6 to 2.6 wt.% [Mg# 0.94-0.96]), Al<sub>2</sub>O<sub>3</sub> (1.45-1.77 wt.%) [Mg# =Mg/(Mg+ΣFe)],  
221 and Cr<sub>2</sub>O<sub>3</sub> (0.25-0.61 wt.%) than the rim (1.2-1.35 wt.% [Mg# 0.97], 0.47-0.52 wt.%, 0.10-  
222 0.13 wt.%, respectively)(Table 1). In both samples, unzoned matrix antigorite has a  
223 composition equivalent to the rim of the elongated antigorite crystals. The Mn# [Mn# =  
224 Mn/(Mn+Fe+Ni)] of antigorite is 0.0006 (±0.0004).

225 The preserved spinel core in sample V18-3a has Cr# [Cr/(Cr+Al)] of 0.79 ±0.001 (Table 2).

226 The mantle overgrowing the primary spinel has a ferritchromite mantle of Cr-magnetite

227 with a Cr# of 0.91 and higher MnO relative to the core. The magnetite rims with no Al<sub>2</sub>O<sub>3</sub>,  
228 but high Cr<sub>2</sub>O<sub>3</sub> (1.87 ±1.16 wt.%). The composition of the disseminated and vein magnetite  
229 differs from magnetite found in the spinel sites, with very little Cr<sub>2</sub>O<sub>3</sub> (Table 2).

230 Diopside in sample V18-3a has a Mg number [Mg# =Mg/(Mg+Fe)] of 0.98. Chlorite in V18-2b  
231 and V18-3a has an Mg# [Mg# =Mg/(Mg+ΣFe)] of 0.95, and Cr<sub>2</sub>O<sub>3</sub> up to 4.07 wt.% (Table 1).

232 Brucite has up to 3 wt.% FeO (as total Fe), Mg# [Mg# =Mg/(Mg+Fe)] of 0.97 (Table 2). Alloys  
233 and sulfides are Ni rich, with various amounts of S, Fe and trace amounts of Pb, Cu, et Co  
234 (Table 3). Alloys mainly consist of Cu-bearing FeNi alloy (taenite) (Table 3). Sulphides include  
235 Ni, Cu, and Fe sulphides. Only heazlewoodite (NiS) was analysed whereas for other  
236 sulphides proper analyses could not be obtain owing to the small grain sizes.

### 237 **3.2. Fluid inclusion analysis**

238 Primary olivine in all samples is rich in fluid inclusions forming secondary trails (Fig. 7). The  
239 fluid inclusion trails are confined within individual crystals and show two alternative  
240 structural relationships relative to the antigorite veins, being either cut by them (Fig. 7A) or  
241 propagating from them (Fig. 7B-C). These patterns suggest a secondary fluid inclusions  
242 entrapment during the antigorite serpentinization event, which appear the dominant  
243 hydration event in the rock.

244 Fluid inclusions of 0.5 to 5 µm in size were analyzed and exhibit rounded to elongated  
245 shapes (Fig. 7D-E). Optical microscope observations at room conditions suggest that the  
246 fluid inclusions are either single-phase and gaseous, or bi-phase with solid and gas.  
247 MicroRaman spectra of fluid inclusions are presented in Fig. 8. The spectra show the

248 presence of marked CH<sub>4</sub> bands (2912 cm<sup>-1</sup>), as well as N<sub>2</sub> (2327 cm<sup>-1</sup>), NH<sub>3</sub> (3324 cm<sup>-1</sup>), S-  
249 H/H<sub>2</sub>S (2575 cm<sup>-1</sup>). Free H<sub>2</sub>O in the fluid inclusions was not detected by MicroRaman.  
250 However, the presence of tiny amounts of free H<sub>2</sub>O in the fluid inclusions —undetectable by  
251 MicroRaman at room conditions— cannot be excluded (Berkesi et al., 2009; Lamadrid et al.,  
252 2017).

253 The molar fraction of gas in the gas mixture was estimated using the Raman scattering  
254 cross-section and the instrumental efficiency of each species. Using equation presented in  
255 Frezzotti *et al.*, 2012, we obtain the following molar proportion: CH<sub>4</sub> = 92±6%, N<sub>2</sub> = 6±5%,  
256 H<sub>2</sub>S = 1±1% and NH<sub>3</sub> = 1±2% for the mean composition of twenty inclusions in olivine from  
257 all samples (supplementary material 1). Composition within the same inclusion trail show  
258 molar fractionation variation smaller than 1% but different trail within the same crystal can  
259 exhibit up to 10% of molar fraction of CH<sub>4</sub> and could reflect fluid heterogeneity.  
260 Alternatively, this effect can be the result of different crystal orientation during data  
261 acquisition (Caumon et al., 2019). No clear pattern was observed linked to relationship  
262 between inclusion trails and antigorite veinlets.

263 Solid phases were identified in large (2-5 μm) fluid inclusions. MicroRaman analysis revealed  
264 the presence of lizardite and brucite but no magnetite was detected. Some inclusions  
265 contain graphite as a solid phase in the inclusion in addition (Fig. 7F and Fig. 8B). The only  
266 sporadic presence of graphite in the fluid inclusions, and in particular in inclusions resulting  
267 from necking processes, suggest that this mineral precipitated as a result of local  
268 respeciation of the fluid inclusions, such as post entrapment host-inclusion reaction with the  
269 inclusion wall and resulting respeciation of the fluid inclusion composition (Cesare, 1995).  
270 This feature is also suggested by the presence of hydrous phases in the inclusions, which

271 indicates interaction of the inclusion fluid with the host olivine. However, the presence of  
272 step-daughter minerals in the inclusion is not systematic, suggesting that the initial fluid was  
273 already rich in CH<sub>4</sub> (-N<sub>2</sub>-NH<sub>3</sub>-H<sub>2</sub>S) at the time of trapping, and that the reduced fluid species  
274 did not form only inside the fluid inclusions.

### 275 **3.3. Rodingites**

276 Rodingites have been identified inside the BMC and consist of garnet, diopside, epidote,  
277 carbonate ± graphite. While not being the focus of this study, the carbonate in the  
278 rodingites has abundant fluid inclusions. Fluid inclusions exhibit negative crystal shape and  
279 are single-phase gaseous at room conditions. The composition of the carbonate-hosted fluid  
280 inclusions, as revealed by Raman spectroscopy, is essentially CH<sub>4</sub> and N<sub>2</sub>. The analyses of the  
281 collected Raman spectra in carbonates (see section 4.3) yield molar fractions of N<sub>2</sub> = 67±4%,  
282 CH<sub>4</sub> = 33±4% on four different inclusions.

### 283 **3.4. Thermodynamic modelling**

284 Thermodynamic calculations were performed in order to constrain the mineralogical, fluid  
285 and redox evolution of the HP serpentinization. The calculations were done at temperatures  
286 consistent with the peak metamorphic conditions estimated for the BMC, i.e., 400 °C to 500  
287 °C and 1 GPa (Honsberger, 2015; Laird et al., 1993), and for different F/R ratios (from 0.5 to  
288 100). The selected partially serpentinized samples are embedded in strongly serpentinized  
289 rocks and, in turn, are included in metasedimentary rocks. For this reason, either ultramafic  
290 or metasedimentary were considered to calculate the EQ3 fluid compositions and as  
291 possible fluid sources responsible for the metamorphic serpentinization of the BMC rocks.  
292 The interaction of EQ3 fluids equilibrated with metasedimentary sources or Si-rich

293 ultramafic sources (e.g. steatite) with the EQ6 dunitic assemblage (cf. Section 2), however,  
294 resulted in mineral assemblages inconsistent with the natural samples (Supplementary  
295 material 2). For this reason, in the following are presented in detail only the results obtained  
296 for EQ3 fluid compositions equilibrated with an ultramafic assemblage consisting of  
297 antigorite + magnetite + brucite + chlorite + olivine. The  $fO_2$  of the infiltrating fluid was set  
298 at the quartz-fayalite-magnetite (QFM) buffer. Figure 10 shows the mineralogical evolution  
299 as a function of reaction progress at 450 °C and 1GPa for a F/R ratio of 1. The model  
300 reaction proceeds with progressive transformation of, from the first to the last reacting  
301 mineral, mantle spinel, clinopyroxene, orthopyroxene, and olivine. Magnetite starts to form  
302 during the early stages of the reaction along with chlorite in response to spinel  
303 consumption. Reaction of mantle pyroxenes marks the precipitation of metamorphic  
304 clinopyroxene (diopside 93%, hedenbergite 3.35% and clino-enstatite 3.65%), metamorphic  
305 olivine, antigorite, and additional magnetite. The late formation of antigorite marks the  
306 partial consumption of metamorphic olivine and a decrease in its Mg#, from Mg# 0.90 to  
307 Mg# 0.83. These patterns reflect the microstructural features observed in the natural  
308 samples. For example, spinel appears intensely replaced by chlorite in rather  
309 unserpentinized portions of the rock (Fig. 9A). Similarly, mantle olivine adjacent to fully  
310 replaced mantle pyroxenes is commonly little affected by the serpentinization. Both mantle  
311 and metamorphic olivine in the natural samples appear texturally replaced by antigorite, as  
312 also suggested by the modelling while approaching reaction completion. With the chosen  
313 bulk composition and used thermodynamic data set, the formation of antigorite is limited to  
314  $T < 470$  °C. The obtained antigorite stability field may be dependent on the absence of iron  
315 in the antigorite thermodynamic model considered in the database. The evolution of  
316 dissolved elements in the fluid (Fig. 9B) indicates that the total Mg content decreases during

317 the reaction, while Si and Ca increase. The  $fO_2$  decreases progressively during the reaction  
318 progress, with a steep decrease during the formation of antigorite down to  $\Delta\text{Log QFM} = -1.2$   
319 (Fig. 9D). Methane, initially about 1 order of magnitude less concentrated than  $CO_2$  in the  
320 reacting fluid, becomes a dominant species at reaction completion (about 1 order of  
321 magnitude more concentrated than  $CO_2$ ). Nevertheless, variations of parameters such as  
322 F/R ratio, mineralogy, or temperature, were found to affect the proportion of  $CH_4$  and  $CO_2$ .  
323 As an example, increasing the modal proportion of either orthopyroxene or clinopyroxene in  
324 the initial rock or decreasing the F/R ratio appears to favor a higher proportion of  $CH_4$  in the  
325 fluid in respect to  $CO_2$ . The model predicts high relative concentration of  $H_2$  in the fluids,  
326 however  $H_2$  was not detected in natural samples by micro-Raman spectroscopy. This may be  
327 due to leakage of  $H_2$  from the inclusions or internal respeciation. Sulphur and nitrogen  
328 speciation were also assessed, with  $HS^-$  and  $H_2S$  and  $NH_3$  being the dominant Sulphur  
329 species relative to  $HSO_4^-$  and  $N_2$  and  $NH_4^+$ , respectively (Fig. 9C).

## 330 **4. Discussion**

### 331 **4.1. Patterns and timing of serpentinization**

332 The timing of serpentinization of slab-derived, exhumed HP serpentinized rocks can span  
333 (sub)seafloor or trench conditions prior to subduction, prograde hydration during  
334 subduction, or retrograde hydration during exhumation. The BMC complex has been  
335 interpreted as a fragment of subducted Iapetus lithosphere, and therefore may have  
336 recorded different stages of serpentinization. Although the possibility of at least some  
337 (sub)seafloor serpentinization prior to the Taconic subduction cannot be excluded, our data  
338 cannot provide any proof of such a pre-subduction event and, instead, suggest a main  
339 hydration event at HP-HT conditions in the subduction zone.

340 Besides late chrysotile veinlets, antigorite is the only serpentine mineral identified in the  
341 BMC rocks. Although formation of antigorite may occur in a wide range of P-T conditions  
342 also as a function of chemical parameters such as the silica activity (Rouméjon et al., 2019),  
343 serpentinites dominated by antigorite are generally referred to the HT temperature part of  
344 the serpentine stability field, generally above ~300-400 °C (e.g., Evans, 2004; Schwartz et  
345 al., 2013). In most subduction zone settings, these conditions also correspond to relatively  
346 HP conditions above 1 GPa. However, the presence of antigorite does not necessarily imply  
347 the serpentinization event to have happened at HP-HT conditions because it could also have  
348 formed as a result of the prograde transformation of lizardite or chrysotile following the  
349 reaction:



351 Nevertheless, several lines of evidence indicate that the BMC rocks recorded a stage of HP-  
352 HT serpentinization. As a first general consideration, the presence of fresh mantle  
353 assemblages throughout the complex (Chidester *et al.*, 1978; this study) represents a  
354 suitable condition to promote HP-HT serpentinization in the subduction zone, if aqueous  
355 fluids are available. Such a process has already been proposed in other HP ultramafic  
356 massifs preserving fresh mantle assemblages (e.g.: Dandar et al., 2019; Früh-Green et al.,  
357 2004; Nozaka, 2018; Scambelluri and Tonarini, 2012; Vitale Brovarone et al., 2020, 2017).  
358 The BMC rocks provides evidence for such a HP hydration event. Figure 10 summarizes the  
359 proposed fluid-rock evolution of the BMC rocks as inferred from the studied samples. The  
360 first indication of serpentinization (stage I in Fig. 10) is suggested by the growth of elongated  
361 metamorphic olivine on the primary clinopyroxene sites (Fig. 5G), which suggests the former  
362 presence of serpentine blades overgrowing the primary clinopyroxene. The selective growth

363 of serpentine at the expense of clinopyroxene rather than primary olivine places this  
364 hypothetical event at HT conditions (Klein et al., 2013) and possibly in the antigorite stability  
365 field (Fig. 11). Metamorphic olivine is most commonly interpreted to form in response of  
366 serpentine dehydration during prograde metamorphism (Plümper et al., 2017; Scambelluri  
367 et al., 1991). Figure 11 provides a compilation of generic antigorite dehydration reactions  
368 leading to the formation of metamorphic olivine. Although these reactions may be shifted to  
369 higher or lower temperatures depending on compositional features (e.g., Padròn-Navarta et  
370 al., 2013), the peak metamorphic conditions proposed for the BMC (0.9-1.3 GPa and 520 °C)  
371 are consistent with the first olivine-forming reaction involving antigorite + brucite as  
372 reactants. Moreover, several studies have shown that olivine can form at T conditions lower  
373 than the reactions shown in Figure 11 as a result of local bulk compositional features  
374 (Plümper et al., 2017). Alternatively, metamorphic olivine after orthopyroxene may also  
375 have formed in response to hydration rather than dehydration reactions, as already  
376 proposed for serpentized mantle wedge rocks (Dandar et al., 2019) following the reaction:

377 Orthopyroxene + 0.46 Water + 0.35 Mg<sup>2+</sup>=

378 0.59 M-olivine + 0.06 Antigorite + 0.29 Silica + 0.7 H<sup>+</sup> (2)

379 The thermodynamic modeling results supports this reaction, as suggested by the decrease  
380 of total dissolved Mg and the increase of Si in the fluid during the early growth of  
381 metamorphic olivine (Fig. 9A and 10B). In either case (hydration or dehydration), the  
382 amount of serpentization predating the formation of metamorphic olivine must have been  
383 very low and, if any, related to a HT event.

384 The second, more robustly constrained stage of transformation (stage II in Fig. 10) is  
385 characterized by the formation of metamorphic olivine after primary orthopyroxene, and as

386 rim around primary clinopyroxene (now recrystallized into diopside). This reaction was  
387 observed in rocks containing rather undisturbed primary olivine, which again point to HT  
388 serpentinization conditions (Klein et al., 2013). The partial preservation of clinopyroxene  
389 exsolution lamellae inside metamorphic olivine pseudomorphic on orthopyroxene may  
390 suggest nearly isovolumetric replacement during this event (Plümper et al., 2012b; Viti et  
391 al., 2005). The thermodynamic modeling results suggest that, at 450 °C and 1 GPa, a  
392 transient antigorite generation may have formed together with metamorphic olivine early in  
393 the fluid-rock interaction, along with spinel breakdown. The Al-Cr-rich antigorite cores  
394 (Atg1) observed in the studied samples may testify to this transient antigorite formation.  
395 Measured distribution coefficients between antigorite and olivine also suggest different  
396 stages of antigorite formation (Supplementary materials 3). The third stage (stage III in Fig.  
397 10) is characterized by the growth of a matrix antigorite (Atg2) at the expense of both  
398 primary and metamorphic olivine. This event may mark either retrograde hydration along  
399 the exhumation path of the BMC, or the progression of the fluid-rock interaction. As  
400 indicated by the thermodynamic modeling results, a second antigorite generation is  
401 expected to form at 450 °C and 1 GPa after the precipitation of metamorphic olivine (Fig.  
402 9A).

403 The fourth stage of serpentinization (IV in Fig. 10) is characterized by the complete  
404 serpentinization of primary olivine and partial to full serpentinization of metamorphic  
405 olivine. The partial preservation of metamorphic olivine after orthopyroxene in sample free  
406 of any primary olivine relict indicates that the largest event of serpentinization of the BMC  
407 rocks took place after the formation of metamorphic olivine. The presence of both  
408 antigorite and chrysotile + brucite at the expense of metamorphic olivine after

409 orthopyroxene suggests that this event protracted during the cooling of the BMC  
410 metamorphic path to temperatures lower than 400 °C (Fig. 11).

411 In summary, based on the collected petrographic and thermodynamic data, the dominant  
412 serpentinization event observed in the BMC complex is interpreted to have taken place in  
413 the Taconic subduction zone.

414

## 415 **4.2. Timing of fluid inclusion formation and origin of CH<sub>4</sub>**

### 416 **4.2.1. Timing of fluid inclusion entrapment**

417 Fluid inclusions in the BMC ultramafic and related metasomatic rocks contain reduced fluid  
418 species such as CH<sub>4</sub>, NH<sub>3</sub>, and H<sub>2</sub>S. The timing of fluid inclusion formation, as well as the  
419 origin of their reduced speciation, is discussed in this section.

420 Reduced fluids have been found to form in ultramafic systems in a wide range of geologic  
421 conditions spanning mid-ocean ridges, obducted ophiolitic massifs, orogenic peridotite  
422 bodies, in subduction, and in the upper mantle (Andréani et al., 2007; Etiope et al., 2011;  
423 Schrenk et al., 2013; Vitale Brovarone et al., 2020). In the BMC rocks, the fluid inclusions  
424 may have formed in three different stages of the evolution of the massif and corresponding  
425 to three different geodynamic settings: (i) in the mantle prior to the formation of the  
426 Iapetus Ocean, (ii) during the (sub)seafloor evolution prior to subduction, and (iii) in the  
427 subduction zone.

428 A primary mantle origin can be ruled out because the observed fluid inclusions occur as  
429 secondary trails propagating from the antigorite veinlets crossing olivine crystal. A  
430 (sub)seafloor origin would match the identification of CH<sub>4</sub>-rich fluid inclusions in oceanic  
431 peridotite (Cannat et al., 2010; Holm and Charlou, 2001). However, in this case, the fluid

432 inclusions would have been preserved during prograde metamorphism to at least 520 °C  
433 and 1 GPa, which is unlikely (Touret, 2001). Moreover, the BMC fluid inclusions are rich in N  
434 species (NH<sub>3</sub>, N<sub>2</sub>), which seems to be an uncommon feature in fluid inclusions from oceanic  
435 peridotites (Grozeva et al., 2020; Klein et al., 2019). Instead, N-rich, NH<sub>3</sub>-bearing fluid  
436 inclusions have been recently documented in CH<sub>4</sub>-rich fluid inclusions in HP serpentized  
437 peridotites from the Alpine belt and proposed to represent a distinctive feature of  
438 subduction zone serpentizing fluids relative to mantle or (sub)seafloor fluids, especially in  
439 the presence of metasediment-derived fluids (Vitale Brovarone et al., 2020). Considering the  
440 microstructural and petrologic features discussed in Section 5.1, and the abundance of N  
441 species, a metamorphic origin in the Taconic subduction is proposed for the studied fluid  
442 inclusions.

443 The formation of lizardite and brucite as step-daughter minerals inside the fluid inclusions  
444 can be interpreted (1) as a prograde, pre-antigorite inclusion-host interactions, (2) as a  
445 retrograde reequilibration of antigorite during cooling of the BMC below ~400 °C with  
446 excess brucite (Reaction 1), or (3) as a retrograde host-inclusion interaction below ~400 °C  
447 (Fig. 11). Excluding lizardite (meta)stability due to local equilibrium/kinetic features or faster  
448 antigorite-lizardite conversion in the inclusions relative to the host rock, we interpret the  
449 formation of step-daughter lizardite and brucite as a retrograde host-inclusion interaction.  
450 Similar interpretations have been proposed for analogous inclusions from Alpine belt (Vitale  
451 Brovarone et al., 2020).

452

#### 453 **4.2.2. Origin of the reducing potential and fluid sources**

454 Another important question is the origin the identified reduced fluids species. In particular,  
455 several studies over the last decades have investigated the biotic or abiotic origin of  
456 geological CH<sub>4</sub> and associated reduced fluid species (Etiope et al., 2011; Etiope and  
457 Sherwood Lollar, 2013; McCollom, 2016; Ménez et al., 2018). Ultramafic systems are  
458 generally favorable environments for the genesis of abiotic CH<sub>4</sub> (Section 5.2.1), but other  
459 interpretations are also possible.

460 For example, the abundance of metasedimentary rocks in the study area may have  
461 promoted the formation of thermogenic gases during their prograde evolution. This  
462 hypothesis would be also consistent with the production of NH<sub>3</sub> through degassing of  
463 organic matter in metasedimentary rocks (Bebout and Fogel, 1992; Li et al., 2009). Biotic  
464 processes, including thermogenic gas formation, typically show very light  $\delta^{13}\text{C}_{\text{CH}_4}$  signatures  
465 (Etiope and Sherwood Lollar, 2013), whereas abiotic processes generally result in much  
466 heavier  $\delta^{13}\text{C}_{\text{CH}_4}$  ( $\sim$ -50 to 0‰) (Etiope and Sherwood Lollar, 2013). In order to test this  
467 hypothesis, we performed reconnaissance  $\delta^{13}\text{C}$  analysis of CH<sub>4</sub> in the fluid inclusions  
468 (Boutier et al., in preparation). The analyses yielded  $\delta^{13}\text{C}$  in the range of -14‰ ( $\pm$ 2‰) for  
469 inclusions in olivine, and -13‰ ( $\pm$ 1‰) for carbonate-hosted methane-rich inclusions from  
470 the rodingites. Even though these results must be considered as preliminary test data, they  
471 seem to exclude the possibility of a pure thermogenic source.

472 Following the hypothesis of an abiotic origin, two possible mechanisms for the formation of  
473 CH<sub>4</sub> can be considered with either external or internal sources, respectively. External  
474 sources correspond to the infiltration of CH<sub>4</sub> and other reduced species formed abiotically in  
475 other geological reservoirs. A deep mantle origin for the reduced fluids detected in the BMC  
476 fluid inclusions appears unlikely if the syn-inclusion, water-rich nature of the serpentinizing

477 fluid is considered. The metasedimentary formations adjacent to the BMC contain  
478 carbonate, graphitic carbon, sulphides, and phyllosilicates as potential sources of the C-N-S-  
479 H fluid identified in the fluid inclusions. Previous studies along the Appalachian belt have  
480 reported evidence of carbon mobilization from these metasedimentary formations or their  
481 along-strike equivalents. For example, Zhang *et al.*, 2018 documented metamorphic loss of  
482 isotopically light carbon from the Wepawaug schists, Connecticut. The possibility for these  
483 carbonate-bearing formations to generate strongly reduced fluids abiotically is not obvious  
484 —for reference, water-maximum conditions in graphite-saturated fluids contain roughly  
485 equal proportions of CH<sub>4</sub> and CO<sub>2</sub> (Connolly, 1995; Holloway, 1984) —. Nevertheless,  
486 evidence for the circulation of CH<sub>4</sub>-rich fluids in equivalent formations in East Central  
487 Vermont and New Hampshire has been reported (Evans *et al.*, 2002; Rumble III and Hoering,  
488 1986). Nevertheless, most petrological studies focusing on New England metasediment-  
489 derived fluids point to more oxidized, CO<sub>2</sub>-dominated aqueous fluids (Ferry, 2007;  
490 Penniston-Dorland and Ferry, 2006). Alternative external sources of reduced fluids would  
491 require unidentified processes, including mixing of different carbon reservoirs, or water-  
492 rock interactions equivalent to those that took place in the BMC.

493 A reducing potential internal to the BMC, and in particular the hydroxylation of fresh mantle  
494 peridotites during the Taconic subduction, appears the most likely interpretation for the  
495 genesis of the identified reduced fluid species. The presence of Fe-Ni alloys in the BMC  
496 partially serpentinized peridotites indicates that the rock recorded reducing conditions, as  
497 already observed in several oceanic and ophiolitic, and some subduction zone serpentinites  
498 (Evans *et al.*, 2017; Frost, 1985; Klein and Bach, 2009; Vitale Brovarone *et al.*, 2020).  
499 Alternatively, reducing fluids may also be produced by serpentinite dehydration (Evans and  
500 Frost, 2021; Piccoli *et al.*, 2019). However, the small amount of metamorphic olivine

501 observed in the BMC rocks seems to contradict this hypothesis. High-pressure syn-  
502 serpentization reducing conditions are also suggested by the thermodynamic modelling  
503 results presented in this study, which indicates  $f_{O_2}$  values as low as  $-3.2 \Delta QFM$  at  $400^\circ C$   
504 and 1 GPa to  $-1.2 \Delta QFM$  at  $450^\circ C$  and 1 GPa, and the formation of significant amounts of  $H_2$   
505 in the fluid (Fig. 9D). The interaction of this  $H_2$  with dissolved carbon, nitrogen, and Sulphur  
506 species present in the serpentizing fluid, could have favored the formation of  $CH_4$ ,  $H_2S$ , and  
507  $NH_3$  from more oxidized species. For  $NH_3$ , the modelling also indicates that this species is  
508 already the dominant N species in the infiltrating fluid buffered at QFM. This feature  
509 suggests that the  $N_2$  detected in the fluid is most likely formed through post-entrapment  
510 respeciation of  $NH_3$ , unless the serpentizing fluid was more oxidized than QFM. The  
511 absence of detectable  $H_2O$  in the fluid inclusions is interpreted to result from host-inclusion  
512 interaction and formation of step-daughter lizardite and brucite, or by the preferential  
513 entrapment of immiscible reduced gases relative to aqueous fluids (Huang et al., 2017;  
514 Vitale Brovarone et al., 2017). The absence of residual  $H_2$  in the fluid inclusions may be  
515 explained by the much faster diffusion  $H_2$  relative to other fluid species through the host  
516 olivine, or by selective leakage.

517 The most plausible sources of serpentizing fluid were the metasedimentary formations  
518 surrounding the BMC complex. These rock types host substantial amounts of subducted  
519 carbon, sulphur, and nitrogen (Bebout and Fogel, 1992; Evans et al., 2014; Kelemen and  
520 Manning, 2015; Plank and Manning, 2019). An ultramafic source internal to the BMC would  
521 not be consistent with the general retention of N during prograde metamorphism and  
522 dehydration of serpentinites (Halama et al., 2014). The hypothesis of a metasediment-  
523 derived serpentizing fluid was also suggested by previous oxygen and hydrogen isotopic  
524 data on antigorite from the BMC complex (Wenner and Taylor, 1974, 1971). Moreover, the

525 authors proposed antigorite-magnetite equilibration T in the range of 220-460 °C, which is  
526 consistent with the prograde P-T of the BMC (Fig. 11). This supports the interpretation of a  
527 subduction-related serpentinization related to the infiltration of metasedimentary-derived  
528 fluids in a rather dry ultramafic body.

## 529 **5. Conclusions**

530 Mineralogical, microstructural, and fluid inclusion study of variably serpentinized dunite  
531 from the Belvidere Mountain Complex, Appalachian belt, Northern Vermont, provides  
532 insight into the process of high-pressure serpentinization in subduction zone and the related  
533 fluid-rock redox patterns. Although the BMC underwent a complex tectonic evolution  
534 potentially characterized by multiple stages of hydration from the (sub)seafloor to  
535 subduction and exhumation, the collected data point to a major event of high-pressure  
536 serpentinization that took place in the Appalachian subduction zone. Metamorphic olivine in  
537 the BMC serpentinized peridotite is interpreted as the product of rock hydration rather than  
538 dehydration, linked to the high-pressure serpentinization event. Our data support the  
539 hypothesis that the methane observed in olivine-hosted secondary fluid inclusions is  
540 genetically linked to serpentinization in the antigorite stability field consistent with the high-  
541 pressure portion of the prograde or retrograde P-T path of the BMC. This favors an abiotic  
542 origin for this methane, even though a biotic origin for the C source cannot be excluded. The  
543 C- and N-rich composition of fluid inclusions suggests a metasediment-derived origin for the  
544 serpentinizing fluid. The high-pressure serpentinization and related abiotic methanogenesis  
545 place the Belvidere mountain complex as a suitable proxy for the study of mantle wedge  
546 serpentinization. This study confirms the importance of fluid mobility in deep seated

547 ultramafic body in subduction zones for the mobility of C, H, and N, and their implications  
548 on large-scale geochemical cycling.

## 549 **6. Acknowledgments**

550 The authors wish to thank Mark Van Baalen for logistic support and fruitful discussion, and  
551 Leslie white for fundamental support during the field work. J.C.M De Hoog is thanked for a  
552 very constructive review on an earlier version of this article. AVB acknowledges a MIUR Rita  
553 Levi Montalcini grant and a Richard Lounsbery Foundation grant. Simona Ferrando is  
554 thanked for her helpful discussions and insights on fluid inclusions. IFP Energies Nouvelles  
555 and its helpful personnel is thanked for its help in the acquisition on test isotopic data of  
556 methane.

557

558 **Fig. 1:** A: *Simplified geological map of Vermont, modified from Hibbard et al., (2006).* B:  
559 *Simplified bedrock geologic map of the Belvidere Mountain Complex and the surrounding*  
560 *formations. Modified after Hibbard et al., (2006). Units description from Hibbard et al.,*  
561 *(2006) and Gale, (2007).*

562 **Fig. 2:** A-B: *Photographs of the Belvidere serpentized peridotite in outcrop.* C: *Weakly*  
563 *serpentized dunite (samples V18-2a and V18-2b).* D: *Serpentized dunite, with boudinaged*  
564 *meta-gabbro (samples V18-3a and V18-3b).*

565 **Fig. 3:** A: *Photomicrograph of a partially serpentized dunite.* B: *Partial replacement of*  
566 *primary chromian spinel by magnetite and chlorite.* C: *Partial replacement of olivine by*  
567 *antigorite.* D: *Inferred primary orthopyroxene being pseudomorphically replaced by*  
568 *metamorphic olivine. See also Figure 5B.* E: *Photomicrograph of a pyroxenite layer included*

569 *in the Belvidere peridotite. The photomicrograph shows radial diopside aggregate*  
570 *pseudomorphic on primary clinopyroxene. Partially serpentinized olivine is also visible. F:*  
571 *Magnetite-rich diopside pseudomorphosis on primary clinopyroxene. Note the growth of*  
572 *metamorphic olivine at the rim of the clinopyroxene site. See Figure 5A for SEM-based*  
573 *backscattered electron image. G: Metamorphic diopside replacing primary clinopyroxene. In*  
574 *this case, note the growth of metamorphic olivine along fractures cutting the*  
575 *pseudomorphosis. See Figure 5F for SEM-based backscattered electron image. H: Relict of*  
576 *metamorphic olivine pseudomorphic on primary clinopyroxene. The metamorphic olivine is*  
577 *then partially replaced by serpentine + brucite + magnetite. A-D: Sample V18-2b, E-G:*  
578 *Sample V18-3a; H: sample V18-B3. P-Ol: primary olivine, M-Ol: metamorphic olivine, Atg:*  
579 *antigorite, Chl: chlorite, Mgt: magnetite, Di: diopside, Chr: chromite, Br: brucite, Ctl:*  
580 *chrysotile.*

581 **Fig. 4:** *Raman spectra of solid phases. A: Antigorite core (Atg1) and rim (Atg2) (see Fig. 5A).*  
582 *B: Brucite.*

583 **Fig. 5:** *SEM-BSE images of samples V18-2b, V18-3a and V18-B3. A: Microstructural patterns*  
584 *of serpentinization. Two generations of serpentine can be observed based on the BSE*  
585 *contrast, a bright core (Atg1) and a dark rim (Atg2). Note also the striped zonation of*  
586 *primary olivine and the formation of metamorphic olivine. B: Replacement of an inferred*  
587 *primary orthopyroxene crystal by metamorphic olivine. The close-up shows the preservation*  
588 *of clinopyroxene relicts interpreted as exsolutions inside the former orthopyroxene. C:*  
589 *Formation of brucite at the expense of metamorphic olivine. D: Composite aggregate of Fe-*  
590 *Ni and Fe-Cu-Ni alloys and Ni sulphide. E: Growth of metamorphic olivine around a diopside-*  
591 *rich primary clinopyroxene pseudomorphosis. A primary chromina spinel partially converted*

592 into magnetite can also be observed. F: Metamorphic diopside replacing primary  
593 clinopyroxene. Note the presence of antigorite + metamorphic olivine  $\pm$  magnetite along the  
594 fractures. In this case, metamorphic olivine occupies the centre of the fractures and is not in  
595 contact with diopside, whereas the metamorphic olivine rimming the primary clinopyroxene  
596 site is in contact with it. G: Metamorphic olivine growing at the expense of metamorphic  
597 diopside (former primary clinopyroxene). The microstructure suggests the former presence of  
598 serpentine needles replacing the clinopyroxene and successively replaced by metamorphic  
599 olivine. Both Atg1 and Atg2 antigorite generations are present. H: Relict of metamorphic  
600 olivine formed at the expense of a primary orthopyroxene site in V18-3b. The metamorphic  
601 olivine is partially converted into brucite + serpentine. P-Ol: primary olivine M-Ol:  
602 metamorphic olivine Px: pyroxene Di: diopside Mtg: magnetite Chr: chromite Atg: antigorite  
603 Br: brucite Ctl: chrysotile NiFeS: nickel and iron sulphite. The presence of antigorite was  
604 confirmed by Raman spectroscopy.

605 **Fig. 6:** Mg# versus MnO (wt%) diagram showing the compositional variation of primary and  
606 metamorphic olivine. The Mn-richest cluster of metamorphic olivine belongs to sample V18-  
607 B3 (fully serpentinized peridotite). Background data from Arai et al., (2012); Dandar et al.,  
608 (2019); Debret et al., (2013); Iyer et al., (2008); Nozaka, (2018); Plümper et al., (2012b);  
609 Scambelluri et al., (1995); Shen et al., (2015).

610 **Fig. 7:** Photomicrographs of methane-rich fluid inclusion trails in olivine from sample V18-2a.  
611 Black arrows indicate fluid inclusion trails. A: Inclusion trail being cut by antigorite veinlets.  
612 B: Inclusion trail limited by antigorite veins. C: Secondary trail of fluid inclusions propagating  
613 from an antigorite veinlet. D: Photomicrograph showing a fluid-inclusion-rich olivine  
614 aggregate. E: Close up of the methane-rich fluid inclusions. F: Close up of a graphite bearing  
615 fluid inclusion (red arrow), as confirmed by Raman spectroscopy in (Fig. 8B).

616 **Fig. 8:** Raman spectra of fluid inclusions and step-daughter solid phases. A: Inclusion  
617 showing a marked CH<sub>4</sub> band and minor peaks of N<sub>2</sub>, NH<sub>3</sub> and S-H bond. Lizardite and brucite  
618 O-H bands are also observed. B: Graphite in fluid inclusions (see Fig. 6D). C: Methane-rich  
619 fluid inclusion with a close up of O-H bonds of lizardite and brucite.

620 **Fig. 9:** Thermodynamic modelling of HP serpentinization of dunite and related mineralogical  
621 and fluid evolution. A: Mineralogical evolution during serpentinization at 450 °C and 1 GPa.  
622 B: Evolution of total dissolved elements in the fluid as a function of the reaction progress  
623 presented in A. C: Evolution of the nitrogen and sulphur fluid speciation as a function of the  
624 reaction progress presented in A. D: Evolution of the fO<sub>2</sub> and H<sub>2</sub>, CH<sub>4</sub>, and CO<sub>2</sub> concentrations  
625 in the fluid as a function of the reaction progress presented in A.

626 **Fig. 10:** Reconstruction of the mineralogical evolution of the BMC partially serpentinized  
627 peridotite. An early step of serpentinization is proposed based on the needle-like growth of  
628 metamorphic olivine on primary clinopyroxene, suggesting the presence of serpentine prior  
629 to the formation of metamorphic olivine. The successive growth of antigorite at the expense  
630 of both primary and metamorphic olivine constrains the main serpentinization event to  
631 metamorphic conditions. Finally, a late serpentinization event is proposed based on the  
632 growth of brucite + antigorite + chrysotile on relict metamorphic. Chr : chromite, P-Ol :  
633 primary olivine, M-Ol : metamorphic olivine, Opx : primary orthopyroxene, Cpx : primary  
634 clinopyroxene, Chl : chlorite, Mgt : magnetite, Atg : antigorite, Di : diopside, Brc : brucite, Ctl  
635 : chrysotile.

636 **Fig. 11:** Simplified stability field of serpentine type minerals and olivine, modified from  
637 Guillot et al., (2015) (see references therein for details on the main reactions). The  
638 retrograde P-T path of BMC from Honsberger, (2015) is also shown for reference. Atg :

639 *antigorite, Brc : brucite; Ctl : chrysotile; Ilm : ilmenite; Ol : olivine; Tlc : talc; Ticl : titanian*  
640 *clinohumite. Diamond graphite transition from Day, (2012).*

641

## 642 **7. References**

- 643 Andréani, M., Mével, C., Boullier, A.-M., Escartin, J., 2007. Dynamic control on serpentine  
644 crystallization in veins: Constraints on hydration processes in oceanic peridotites. *Geochem.*  
645 *Geophys. Geosystems* 8.
- 646 Andréani, M., Munoz, M., Marcaillou, C., Delacour, A., 2013.  $\mu$ XANES study of iron redox state in  
647 serpentine during oceanic serpentinization. *Lithos* 178, 70–83.
- 648 Arai, S., Ishimaru, S., Mizukami, T., 2012. Methane and propane micro-inclusions in olivine in  
649 titanoclinohumite-bearing dunites from the Sanbagawa high-P metamorphic belt, Japan:  
650 Hydrocarbon activity in a subduction zone and Ti mobility. *Earth Planet. Sci. Lett.* 353, 1–11.
- 651 Auzende, A.-L., Daniel, I., Reynard, B., Lemaire, C., Guyot, F., 2004. High-pressure behaviour of  
652 serpentine minerals: a Raman spectroscopic study. *Phys. Chem. Miner.* 31, 269–277.
- 653 Bebout, G.E., Fogel, M.L., 1992. Nitrogen-isotope compositions of metasedimentary rocks in the  
654 Catalina Schist, California: implications for metamorphic devolatilization history. *Geochim.*  
655 *Cosmochim. Acta* 56, 2839–2849.
- 656 Bebout, G.E., Penniston-Dorland, S.C., 2016. Fluid and mass transfer at subduction interfaces—The  
657 field metamorphic record. *Lithos* 240–243, 228–258.  
658 <https://doi.org/10.1016/j.lithos.2015.10.007>
- 659 Berkesi, M., Hidas, K., Guzmics, T., Dubessy, J., Bodnar, R.J., Szabó, C., Vajna, B., Tsunogae, T., 2009.  
660 Detection of small amounts of H<sub>2</sub>O in CO<sub>2</sub>-rich fluid inclusions using Raman spectroscopy. *J.*  
661 *Raman Spectrosc. Int. J. Orig. Work Asp. Raman Spectrosc. High. Order Process. Also*  
662 *Brillouin Rayleigh Scatt.* 40, 1461–1463.
- 663 Berman, R.G., 1988. Internally-consistent thermodynamic data for minerals in the system Na<sub>2</sub>O-K<sub>2</sub>O-  
664 CaO-MgO-FeO-Fe<sub>2</sub>O<sub>3</sub>-Al<sub>2</sub>O<sub>3</sub>-SiO<sub>2</sub>-TiO<sub>2</sub>-H<sub>2</sub>O-CO<sub>2</sub>. *J. Petrol.* 29, 445–522.
- 665 Berndt, M.E., Allen, D.E., Seyfried Jr, W.E., 1996. Reduction of CO<sub>2</sub> during serpentinization of olivine  
666 at 300 C and 500 bar. *Geology* 24, 351–354.
- 667 Cannat, M., Fontaine, F., Escartin, J., 2010. Serpentinization and associated hydrogen and methane  
668 fluxes at slow spreading ridges. *Divers. Hydrothermal Syst. Slow Spreading Ocean Ridges*  
669 188, 241–264.
- 670 Castonguay, S., Kim, J., Thompson, P.J., Gale, M.H., Joyce, N., Laird, J., Doolan, B.L., 2012. Timing of  
671 tectonometamorphism across the Green Mountain anticlinorium, northern Vermont  
672 Appalachians: 40Ar/39Ar data and correlations with southern Quebec. *GSA Bull.* 124, 352–  
673 367. <https://doi.org/10.1130/B30487.1>
- 674 Caumon, M.-C., Tarantola, A., Wang, W., 2019. Raman spectra of gas mixtures in fluid inclusions:  
675 Effect of quartz birefringence on composition measurement. *J. Raman Spectrosc.*
- 676 Cesare, B., 1995. Graphite precipitation in C—O—H fluid inclusions: closed system compositional and  
677 density changes, and thermobarometric implications. *Contrib. Mineral. Petrol.* 122, 25–33.
- 678 Chew, D.M., van Staal, C.R., 2014. The ocean–continent transition zones along the Appalachian–  
679 Caledonian Margin of Laurentia: Examples of large-scale hyperextension during the opening  
680 of the Iapetus Ocean. *Geosci. Can.* 41, 165–185.
- 681 Chidester, A.H., Albee, A.L., Cady, W.M., 1978. Petrology, structure, and genesis of the asbestos-  
682 bearing ultramafic rocks of the Belvidere Mountain area in Vermont. *US Govt. Print. Off.*,.

683 Connolly, J.A.D., 1995. Phase diagram methods for graphitic rocks and application to the system C-  
684 O- H- FeO- TiO<sub>2</sub>- SiO<sub>2</sub>. *Contrib. Mineral. Petrol.* 119, 94–116.

685 Dandar, O., Okamoto, A., Uno, M., Oyanagi, R., Nagaya, T., Burenjargal, U., Miyamoto, T., Tsuchiya,  
686 N., 2019. Formation of secondary olivine after orthopyroxene during hydration of mantle  
687 wedge: evidence from the Khantaishir Ophiolite, western Mongolia. *Contrib. Mineral. Petrol.*  
688 174, 86.

689 Debret, B., Nicollet, C., Andreani, M., Schwartz, S., Godard, M., 2013. Three steps of serpentinization  
690 in an eclogitized oceanic serpentinization front (Lanzo Massif–Western Alps). *J. Metamorph.*  
691 *Geol.* 31, 165–186.

692 Deschamps, F., Godard, M., Guillot, S., Hattori, K., 2013. Geochemistry of subduction zone  
693 serpentinites: A review. *Lithos* 178, 96–127.

694 Doolan, B.L., Gale, M.H., Gale, P.N., Hoar, R.S., St-Julien, P., 1982. Geology of the Quebec re-entrant:  
695 possible constraints from early rifts and the Vermont-Quebec serpentine belt. *Major Struct.*  
696 *Zones Faults North. Appalach. Ed. P St-Julien J Béland Geol. Assoc. Can. Spec. Pap.* 24, 87–  
697 115.

698 Etiope, G., Schoell, M., Hosgörmez, H., 2011. Abiotic methane flux from the Chimaera seep and  
699 Tekirova ophiolites (Turkey): understanding gas exhalation from low temperature  
700 serpentinization and implications for Mars. *Earth Planet. Sci. Lett.* 310, 96–104.

701 Etiope, G., Sherwood Lollar, B., 2013. Abiotic methane on Earth. *Rev. Geophys.* 51, 276–299.

702 Evans, B.W., 2010. Lizardite versus antigorite serpentinite: Magnetite, hydrogen, and life (?).  
703 *Geology* 38, 879–882.

704 Evans, B.W., 2004. The serpentinite multisystem revisited: chrysotile is metastable. *Int. Geol. Rev.*  
705 46, 479–506.

706 Evans, K.A., Bickle, M.J., Skelton, A.D.L., Hall, M., Chapman, H., 2002. Reductive deposition of  
707 graphite at lithological margins in East Central Vermont: a Sr, C and O isotope study. *J.*  
708 *Metamorph. Geol.* 20, 781–798.

709 Evans, K.A., Frost, B.R., 2021. Deserpentinization in Subduction Zones as a Source of Oxidation in  
710 Arcs: A Reality Check. *J. Petrol.*

711 Evans, K.A., Reddy, S.M., Tomkins, A.G., Crossley, R.J., Frost, B.R., 2017. Effects of geodynamic  
712 setting on the redox state of fluids released by subducted mantle lithosphere. *Lithos* 278–  
713 281, 26–42. <https://doi.org/10.1016/j.lithos.2016.12.023>

714 Evans, K.A., Tomkins, A.G., Cliff, J., Fiorentini, M.L., 2014. Insights into subduction zone sulfur  
715 recycling from isotopic analysis of eclogite-hosted sulfides. *Chem. Geol.* 365, 1–19.

716 Ferry, J.M., 2007. The role of volatile transport by diffusion and dispersion in driving biotite-forming  
717 reactions during regional metamorphism of the Gile Mountain Formation, Vermont. *Am.*  
718 *Mineral.* 92, 1288–1302.

719 Frezzotti, M.L., Tecce, F., Casagli, A., 2012. Raman spectroscopy for fluid inclusion analysis. *J.*  
720 *Geochem. Explor.* 112, 1–20.

721 Frost, B.R., 1985. On the stability of sulfides, oxides, and native metals in serpentinite. *J. Petrol.* 26,  
722 31–63.

723 Frost, B.R., Beard, J.S., 2007. On silica activity and serpentinization. *J. Petrol.* 48, 1351–1368.

724 Früh-Green, G.L., Connolly, J.A., Plas, A., Kelley, D.S., Grobéty, B., 2004. Serpentinization of oceanic  
725 peridotites: implications for geochemical cycles and biological activity. *Subseafloor*  
726 *Biosphere -Ocean Ridges* 144, 119–136.

727 Gale, M.H., 2007. Bedrock Geologic Map of the Hazens Notch and Portions of the Eden and Lowell  
728 Quadrangles, Vermont. *Vt. Geol. Surv., Vermont geological open file report VG07-2, plate 1.*

729 Gale, M.H., 1986. Geologic map of the Belvidere Mountain area, Eden and Lowell, Vermont (USGS  
730 Numbered Series No. 1560), IMAP.

731 Gale, M.H., 1980. Geology of the Belvidere Mountain Complex, Eden and Lowell, Vermont. US  
732 Geological Survey,.

733 Gonzalez, J.P., Baldwin, S.L., Thomas, J.B., Nachlas, W.O., Fitzgerald, P.G., 2020. Evidence for  
734 ultrahigh-pressure metamorphism discovered in the Appalachian orogen. *Geology* 48, 947–  
735 951.

736 Grozeva, N.G., Klein, F., Seewald, J.S., Sylva, S.P., 2020. Chemical and isotopic analyses of  
737 hydrocarbon-bearing fluid inclusions in olivine-rich rocks. *Philos. Trans. R. Soc. A* 378,  
738 20180431.

739 Guillot, S., Hattori, K.H., de Sigoyer, J., 2000. Mantle wedge serpentinization and exhumation of  
740 eclogites: insights from eastern Ladakh, northwest Himalaya. *Geology* 28, 199–202.

741 Guillot, S., Schwartz, S., Reynard, B., Agard, P., Prigent, C., 2015. Tectonic significance of  
742 serpentinites. *Tectonophysics* 646, 1–19.

743 Halama, R., Bebout, G.E., John, T., Scambelluri, M., 2014. Nitrogen recycling in subducted mantle  
744 rocks and implications for the global nitrogen cycle. *Int. J. Earth Sci.* 103, 2081–2099.

745 Hibbard, J.P., Van Staal, C.R., Rankin, D.W., Williams, H., 2006. Lithotectonic map of the Appalachian  
746 orogen, Canada–United States of America. *Geol. Surv. Can. Map A* 2096, 2.

747 Holloway, J.R., 1984. Graphite-CH<sub>4</sub>-H<sub>2</sub>O-CO<sub>2</sub> equilibria at low-grade metamorphic conditions.  
748 *Geology* 12, 455–458.

749 Holm, N.G., Charlou, J.L., 2001. Initial indications of abiogenic formation of hydrocarbons in the  
750 Rainbow ultramafic hydrothermal system, Mid-Atlantic Ridge. *Earth Planet. Sci. Lett.* 191, 1–  
751 8.

752 Honsberger, I.W., 2015. Metamorphism, deformation, geochemistry, and tectonics of exhumed  
753 ultramafic and mafic rocks in the central and north-central Vermont Appalachians.

754 Honsberger, I.W., Laird, J., Thompson, P.J., 2017. A tectonized ultramafic-mafic-pelitic package in  
755 Stockbridge, Vermont: Metamorphism resulting from subduction and exhumation. *Am. J.*  
756 *Sci.* 317, 1019–1047.

757 Huang, F., Daniel, I., Cardon, H., Montagnac, G., Sverjensky, D.A., 2017. Immiscible hydrocarbon  
758 fluids in the deep carbon cycle. *Nat. Commun.* 8, 1–8.

759 Iyer, K., Austrheim, H., John, T., Jamtveit, B., 2008. Serpentinization of the oceanic lithosphere and  
760 some geochemical consequences: constraints from the Leka Ophiolite Complex, Norway.  
761 *Chem. Geol.* 249, 66–90.

762 Karabinos, P., Samson, S.D., Hepburn, J.C., Stoll, H.M., 1998. Taconian orogeny in the New England  
763 Appalachians: Collision between Laurentia and the Shelburne Falls arc. *Geology* 26, 215–218.  
764 [https://doi.org/10.1130/0091-7613\(1998\)026<0215:TOITNE>2.3.CO;2](https://doi.org/10.1130/0091-7613(1998)026<0215:TOITNE>2.3.CO;2)

765 Kelemen, P.B., Manning, C.E., 2015. Reevaluating carbon fluxes in subduction zones, what goes  
766 down, mostly comes up. *Proc. Natl. Acad. Sci.* 112, E3997–E4006.  
767 <https://doi.org/10.1073/pnas.1507889112>

768 Kelley, D.S., Karson, J.A., Früh-Green, G.L., Yoerger, D.R., Shank, T.M., Butterfield, D.A., Hayes, J.M.,  
769 Schrenk, M.O., Olson, E.J., Proskurowski, G., Jakuba, M., Bradley, A., Larson, B., Ludwig, K.,  
770 Glickson, D., Buckman, K., Bradley, A.S., Brazelton, W.J., Roe, K., Elend, M.J., Delacour, A.,  
771 Bernasconi, S.M., Lilley, M.D., Baross, J.A., Summons, R.E., Sylva, S.P., 2005. A Serpentinite-  
772 Hosted Ecosystem: The Lost City Hydrothermal Field. *Science* 307, 1428–1434.  
773 <https://doi.org/10.1126/science.1102556>

774 Kempf, E.D., Hermann, J., 2018. Hydrogen incorporation and retention in metamorphic olivine  
775 during subduction: Implications for the deep water cycle. *Geology* 46, 571–574.

776 Klein, F., Bach, W., 2009. Fe–Ni–Co–O–S phase relations in peridotite–seawater interactions. *J.*  
777 *Petrol.* 50, 37–59.

778 Klein, F., Bach, W., Humphris, S.E., Kahl, W.-A., Jöns, N., Moskowitz, B., Berquó, T.S., 2014. Magnetite  
779 in seafloor serpentinite—Some like it hot. *Geology* 42, 135–138.

780 Klein, F., Bach, W., McCollom, T.M., 2013. Compositional controls on hydrogen generation during  
781 serpentinization of ultramafic rocks. *Lithos* 178, 55–69.

782 Klein, F., Grozeva, N.G., Seewald, J.S., 2019. Abiogenic methane synthesis and serpentinization in  
783 olivine-hosted fluid inclusions. *Proc. Natl. Acad. Sci.* 116, 17666–17672.

784 Laird, J., Lanphere, M.A., Albee, A.L., 1984. Distribution of Ordovician and Devonian metamorphism  
785 in mafic and pelitic schists from northern Vermont. *Am. J. Sci.* 284, 376–413.

786 Laird, J., Trzcieski, W.E., Bothner, W.A., Cheney, J.T., Hepburn, J.C., 1993. High-pressure, Taconian,  
787 and subsequent polymetamorphism of southern Quebec and northern Vermont. *Contrib.*  
788 *Dep. Univ. Mass.* 67, 1–32.

789 Lamadrid, H.M., Rimstidt, J.D., Schwarzenbach, E.M., Klein, F., Ulrich, S., Dolocan, A., Bodnar, R.J.,  
790 2017. Effect of water activity on rates of serpentinization of olivine. *Nat. Commun.* 8, 1–9.

791 Li, L., Cartigny, P., Ader, M., 2009. Kinetic nitrogen isotope fractionation associated with thermal  
792 decomposition of NH<sub>3</sub>: Experimental results and potential applications to trace the origin of  
793 N<sub>2</sub> in natural gas and hydrothermal systems. *Geochim. Cosmochim. Acta* 73, 6282–6297.

794 Majumdar, A.S., Hövelmann, J., Vollmer, C., Berndt, J., Mondal, S.K., Putnis, A., 2016. Formation of  
795 Mg-rich olivine pseudomorphs in serpentinized dunite from the Mesoarchean Nuasahi  
796 Massif, Eastern India: Insights into the evolution of fluid composition at the mineral–fluid  
797 interface. *J. Petrol.* 57, 3–26.

798 McCollom, T.M., 2016. Abiotic methane formation during experimental serpentinization of olivine.  
799 *Proc. Natl. Acad. Sci.* 113, 13965–13970.

800 Ménez, B., Pisapia, C., Andreani, M., Jamme, F., Vanbellingen, Q.P., Brunelle, A., Richard, L., Dumas,  
801 P., Réfrégiers, M., 2018. Abiotic synthesis of amino acids in the recesses of the oceanic  
802 lithosphere. *Nature* 564, 59–63. <https://doi.org/10.1038/s41586-018-0684-z>

803 Mével, C., 2003. Serpentinization of abyssal peridotites at mid-ocean ridges. *Comptes Rendus*  
804 *Geosci.* 335, 825–852.

805 Moody, J.B., 1976. Serpentinization: a review. *Lithos* 9, 125–138.

806 Nozaka, T., 2018. Compositional variation of olivine related to high–temperature serpentinization of  
807 peridotites: Evidence from the Oeyama ophiolite. *J. Mineral. Petrol. Sci.* 180420.

808 Nozaka, T., 2003. Compositional heterogeneity of olivine in thermally metamorphosed serpentinite  
809 from Southwest Japan. *Am. Mineral.* 88, 1377–1384.

810 Penniston-Dorland, S.C., Ferry, J.M., 2006. Development of spatial variations in reaction progress  
811 during regional metamorphism of micaceous carbonate rocks, northern New England. *Am. J.*  
812 *Sci.* 306, 475–524.

813 Piccoli, F., Hermann, J., Pettke, T., Connolly, J.A.D., Kempf, E.D., Duarte, J.V., 2019. Subducting  
814 serpentinites release reduced, not oxidized, aqueous fluids. *Sci. Rep.* 9, 1–7.

815 Plank, T., Manning, C.E., 2019. Subducting carbon. *Nature* 574, 343–352.

816 Plümpner, O., John, T., Podladchikov, Y.Y., Vrijmoed, J.C., Scambelluri, M., 2017. Fluid escape from  
817 subduction zones controlled by channel-forming reactive porosity. *Nat. Geosci.* 10, 150–156.  
818 <https://doi.org/10.1038/ngeo2865>

819 Plümpner, O., King, H.E., Vollmer, C., Ramasse, Q., Jung, H., Austrheim, H., 2012a. The legacy of  
820 crystal-plastic deformation in olivine: high-diffusivity pathways during serpentinization.  
821 *Contrib. Mineral. Petrol.* 163, 701–724.

822 Plümpner, O., Piazzolo, S., Austrheim, H., 2012b. Olivine pseudomorphs after serpentinized  
823 orthopyroxene record transient oceanic lithospheric mantle dehydration (Leka Ophiolite  
824 Complex, Norway). *J. Petrol.* 53, 1943–1968.

825 Rouméjon, S., Andreani, M., Früh-Green, G.L., 2019. Antigorite crystallization during oceanic  
826 retrograde serpentinization of abyssal peridotites. *Contrib. Mineral. Petrol.* 174, 60.

827 Rumble III, D., Hoering, T.C., 1986. Carbon isotope geochemistry of graphite vein deposits from New  
828 Hampshire, USA. *Geochim. Cosmochim. Acta* 50, 1239–1247.

829 Scambelluri, M., Müntener, O., Hermann, J., Piccardo, G.B., Trommsdorff, V., 1995. Subduction of  
830 water into the mantle: history of an Alpine peridotite. *Geology* 23, 459–462.

831 Scambelluri, M., Strating, E.H., Piccardo, G.B., Vissers, R.L.M., Rampone, E., 1991. Alpine olivine-and  
832 titanian clinohumite-bearing assemblages in the Erro-Tobbio peridotite (Voltri Massif, NW  
833 Italy). *J. Metamorph. Geol.* 9, 79–91.

834 Scambelluri, M., Tonarini, S., 2012. Boron isotope evidence for shallow fluid transfer across  
835 subduction zones by serpentinized mantle. *Geology* 40, 907–910.

836 Schrenk, M.O., Brazelton, W.J., Lang, S.Q., 2013. Serpentinization, carbon, and deep life. *Rev.*  
837 *Mineral. Geochem.* 75, 575–606.

838 Schwartz, S., Guillot, S., Reynard, B., Lafay, R., Debret, B., Nicollet, C., Lanari, P., Auzende, A.L., 2013.  
839 Pressure–temperature estimates of the lizardite/antigorite transition in high pressure  
840 serpentinites. *Lithos* 178, 197–210.

841 Seyfried Jr, W.E., Foustoukos, D.I., Fu, Q., 2007. Redox evolution and mass transfer during  
842 serpentinization: An experimental and theoretical study at 200 C, 500 bar with implications  
843 for ultramafic-hosted hydrothermal systems at Mid-Ocean Ridges. *Geochim. Cosmochim.*  
844 *Acta* 71, 3872–3886.

845 Shen, T., Hermann, J., Zhang, L., Lü, Z., Padrón-Navarta, J.A., Xia, B., Bader, T., 2015. UHP  
846 metamorphism documented in Ti-chondrodite-and Ti-clinohumite-bearing serpentinized  
847 ultramafic rocks from Chinese southwestern Tianshan. *J. Petrol.* 56, 1425–1458.

848 Sleep, N.H., Bird, D.K., 2007. Niches of the pre-photosynthetic biosphere and geologic preservation  
849 of Earth’s earliest ecology. *Geobiology* 5, 101–117.

850 Stanley, R.S., Roy, D.L., Hatch, N.L., Knapp, D.A., 1984. Evidence for tectonic emplacement of  
851 ultramafic and associated rocks in the pre-Silurian eugeoclinal belt of western New England;  
852 vestiges of an ancient accretionary wedge. *Am. J. Sci.* 284, 559–595.  
853 <https://doi.org/10.2475/ajs.284.4-5.559>

854 Sverjensky, D.A., Harrison, B., Azzolini, D., 2014. Water in the deep Earth: the dielectric constant and  
855 the solubilities of quartz and corundum to 60 kb and 1200 C. *Geochim. Cosmochim. Acta*  
856 129, 125–145.

857 Touret, J.L.R., 2001. Fluids in metamorphic rocks. *Lithos* 55, 1–25.

858 Van Baalen, M.R., Mossman, B.T., Gunter, M.E., Francis, C.A., 2009. Environmental Geology of  
859 Belvidere Mt.

860 Vitale Brovarone, A., Martinez, I., Elmaleh, A., Compagnoni, R., Chaduteau, C., Ferraris, C., Esteve, I.,  
861 2017. Massive production of abiotic methane during subduction evidenced in  
862 metamorphosed ophicarbonates from the Italian Alps. *Nat. Commun.* 8, 14134.

863 Vitale Brovarone, A., Sverjensky, D.A., Piccoli, F., Ressico, F., Giovannelli, D., Daniel, I., 2020.  
864 Subduction hides high-pressure sources of energy that may feed the deep subsurface  
865 biosphere. *Nat. Commun.* 11, 1–11.

866 Viti, C., Mellini, M., Rumori, C., 2005. Exsolution and hydration of pyroxenes from partially  
867 serpentinized harzburgites. *Mineral. Mag.* 69, 491–507.

868 Wada, I., Wang, K., He, J., Hyndman, R.D., 2008. Weakening of the subduction interface and its  
869 effects on surface heat flow, slab dehydration, and mantle wedge serpentinization. *J.*  
870 *Geophys. Res. Solid Earth* 113.

871 Wenner, D.B., Taylor, H.P., 1974. D/H and O<sup>18</sup>/O<sup>16</sup> studies of serpentinization of ultramafic rocks.  
872 *Geochim. Cosmochim. Acta* 38, 1255–1286.

873 Wenner, D.B., Taylor, H.P., 1971. Temperatures of serpentinization of ultramafic rocks based on O  
874 18/O 16 fractionation between coexisting serpentine and magnetite. *Contrib. Mineral.*  
875 *Petrol.* 32, 165–185.

876 Wolery, Tj., Jarek, R.L., 2003. Software user’s manual: EQ3/6, version 8.0. *Softw. Doc.* 8–0.

877 Zhang, S., Ague, J.J., Vitale Brovarone, A., 2018. Degassing of organic carbon during regional  
878 metamorphism of pelites, Wepawaug Schist, Connecticut, USA. *Chem. Geol.* 490, 30–44.  
879 <https://doi.org/10.1016/j.chemgeo.2018.05.003>

880

1 **Fig. 1:** A: Simplified geological map of Vermont, modified from Hibbard et al., (2006). B:  
2 Simplified bedrock geologic map of the Belvidere Mountain Complex and the surrounding  
3 formations. Modified after Hibbard et al., (2006). Units description from Hibbard et al., (2006)  
4 and Gale, (2007).

5 **Fig. 2:** A-B: Photographs of the Belvidere serpentized peridotite in outcrop. C: Weakly  
6 serpentized dunite (samples V18-2a and V18-2b). D: Serpentized dunite, with boudinaged  
7 meta-gabbro (samples V18-3a and V18-3b).

8 **Fig. 3:** A: Photomicrograph of a partially serpentized dunite. B: Partial replacement of  
9 primary chromian spinel by magnetite and chlorite. C: Partial replacement of olivine by  
10 antigorite. D: Inferred primary orthopyroxene being pseudomorphically replaced by  
11 metamorphic olivine. See also Figure 5B. E: Photomicrograph of a pyroxenite layer included in  
12 the Belvidere peridotite. The photomicrograph shows radial diopside aggregate  
13 pseudomorphic on primary clinopyroxene. Partially serpentized olivine is also visible. F:  
14 Magnetite-rich diopside pseudomorphosis on primary clinopyroxene. Note the growth of  
15 metamorphic olivine at the rim of the clinopyroxene site. See Figure 5A for SEM-based  
16 backscattered electron image. G: Metamorphic diopside replacing primary clinopyroxene. In  
17 this case, note the growth of metamorphic olivine along fractures cutting the  
18 pseudomorphosis. See Figure 5F for SEM-based backscattered electron image. H: Relict of  
19 metamorphic olivine pseudomorphic on primary clinopyroxene. The metamorphic olivine is  
20 then partially replaced by serpentine + brucite + magnetite. A-D: Sample V18-2b, E-G: Sample  
21 V18-3a; H: sample V18-B3. P-Ol: primary olivine, M-Ol: metamorphic olivine, Atg: antigorite,  
22 Chl: chlorite, Mgt: magnetite, Di: diopside, Chr: chromite, Br: brucite, Ctl: chrysotile.

23 **Fig. 4:** Raman spectra of solid phases. A: Antigorite core (Atg1) and rim (Atg2) (see Fig. 5A). B:  
24 Brucite.

25 **Fig. 5:** SEM-BSE images of samples V18-2b, V18-3a and V18-B3. A: Microstructural patterns of  
26 serpentinization. Two generations of serpentine can be observed based on the BSE contrast, a  
27 bright core (Atg1) and a dark rim (Atg2). Note also the striped zonation of primary olivine and  
28 the formation of metamorphic olivine. B: Replacement of an inferred primary orthopyroxene  
29 crystal by metamorphic olivine. The close-up shows the preservation of clinopyroxene relicts  
30 interpreted as exsolutions inside the former orthopyroxene. C: Formation of brucite at the  
31 expense of metamorphic olivine. D: Composite aggregate of Fe-Ni and Fe-Cu-Ni alloys and Ni  
32 sulphide. E: Growth of metamorphic olivine around a diopside-rich primary clinopyroxene  
33 pseudomorphosis. A primary chromite spinel partially converted into magnetite can also be  
34 observed. F: Metamorphic diopside replacing primary clinopyroxene. Note the presence of  
35 antigorite + metamorphic olivine ± magnetite along the fractures. In this case, metamorphic  
36 olivine occupies the centre of the fractures and is not in contact with diopside, whereas the  
37 metamorphic olivine rimming the primary clinopyroxene site is in contact with it. G:  
38 Metamorphic olivine growing at the expense of metamorphic diopside (former primary  
39 clinopyroxene). The microstructure suggests the former presence of serpentine needles  
40 replacing the clinopyroxene and successively replaced by metamorphic olivine. Both Atg1 and  
41 Atg2 antigorite generations are present. H: Relict of metamorphic olivine formed at the  
42 expense of a primary orthopyroxene site in V18-3b. The metamorphic olivine is partially  
43 converted into brucite + serpentine. P-Ol: primary olivine M-Ol: metamorphic olivine Px:  
44 pyroxene Di: diopside Mtg: magnetite Chr: chromite Atg: antigorite Br: brucite Ctl: chrysotile  
45 NiFeS: nickel and iron sulphite. The presence of antigorite was confirmed by Raman  
46 spectroscopy.

47 **Fig. 6:** Mg# versus MnO (wt%) diagram showing the compositional variation of primary and  
48 metamorphic olivine. The Mn-richest cluster of metamorphic olivine belongs to sample V18-  
49 B3 (fully serpentinized peridotite). Background data from Arai et al., (2012); Dandar et al.,  
50 (2019); Debret et al., (2013); Iyer et al., (2008); Nozaka, (2018); Plümper et al., (2012b);  
51 Scambelluri et al., (1995); Shen et al., (2015).

52 **Fig. 7:** Photomicrographs of methane-rich fluid inclusion trails in olivine from sample V18-2a.  
53 Black arrows indicate fluid inclusion trails. A: Inclusion trail being cut by antigorite veinlets. B:  
54 Inclusion trail limited by antigorite veins. C: Secondary trail of fluid inclusions propagating  
55 from an antigorite veinlet. D: Photomicrograph showing a fluid-inclusion-rich olivine  
56 aggregate. E: Close up of the methane-rich fluid inclusions. F: Close up of a graphite bearing  
57 fluid inclusion (red arrow), as confirmed by Raman spectroscopy in (Fig. 8B).

58 **Fig. 8:** Raman spectra of fluid inclusions and step-daughter solid phases. A: Inclusion showing  
59 a marked CH<sub>4</sub> band and minor peaks of N<sub>2</sub> NH<sub>3</sub> and S-H bond. Lizardite and brucite O-H bands  
60 are also observed. B: Graphite in fluid inclusions (see Fig. 6D). C: Methane-rich fluid inclusion  
61 with a close up of O-H bonds of lizardite and brucite.

62 **Fig. 9:** Thermodynamic modelling of HP serpentinization of dunite and related mineralogical  
63 and fluid evolution. A: Mineralogical evolution during serpentinization at 450 °C and 1 GPa. B:  
64 Evolution of total dissolved elements in the fluid as a function of the reaction progress  
65 presented in A. C: Evolution of the nitrogen and sulphur fluid speciation as a function of the  
66 reaction progress presented in A. D: Evolution of the fO<sub>2</sub> and H<sub>2</sub>, CH<sub>4</sub>, and CO<sub>2</sub> concentrations  
67 in the fluid as a function of the reaction progress presented in A.

68 **Fig. 10:** Reconstruction of the mineralogical evolution of the BMC partially serpentinized  
69 peridotite. An early step of serpentinization is proposed based on the needle-like growth of

70 metamorphic olivine on primary clinopyroxene, suggesting the presence of serpentine prior to  
71 the formation of metamorphic olivine. The successive growth of antigorite at the expense of  
72 both primary and metamorphic olivine constrains the main serpentinization event to  
73 metamorphic conditions. Finally, a late serpentinization event is proposed based on the  
74 growth of brucite + antigorite + chrysotile on relict metamorphic. Chr : chromite, P-Ol : primary  
75 olivine, M-Ol : metamorphic olivine, Opx : primary orthopyroxene, Cpx : primary clinopyroxene,  
76 Chl : chlorite, Mgt : magnetite, Atg : antigorite, Di : diopside, Brc : brucite, Ctl : chrysotile.

77 **Fig. 11:** Simplified stability field of serpentine type minerals and olivine, modified from Guillot  
78 et al., (2015) (see references therein for details on the main reactions). The retrograde P-T  
79 path of BMC from Honsberger, (2015) is also shown for reference. Atg : antigorite, Brc :  
80 brucite; Ctl : chrysotile; Ilm : ilmenite; Ol : olivine; Tlc : talc; Ticl : titanian clinohumite. Diamond  
81 graphite transition from Day, (2012).

## 82 References:

- 83 Arai, S., Ishimaru, S., Mizukami, T., 2012. Methane and propane micro-inclusions in olivine in  
84 titanoclinohumite-bearing dunites from the Sanbagawa high-P metamorphic belt,  
85 Japan: Hydrocarbon activity in a subduction zone and Ti mobility. Earth Planet. Sci.  
86 Lett. 353, 1–11.
- 87 Dandar, O., Okamoto, A., Uno, M., Oyanagi, R., Nagaya, T., Burenjargal, U., Miyamoto, T.,  
88 Tsuchiya, N., 2019. Formation of secondary olivine after orthopyroxene during  
89 hydration of mantle wedge: evidence from the Khantaishir Ophiolite, western  
90 Mongolia. Contrib. Mineral. Petrol. 174, 86.
- 91 Day, H.W., 2012. A revised diamond-graphite transition curve. Am. Mineral. 97, 52–62.
- 92 Debret, B., Nicollet, C., Andreani, M., Schwartz, S., Godard, M., 2013. Three steps of  
93 serpentinization in an eclogitized oceanic serpentinization front (Lanzo Massif–  
94 Western Alps). J. Metamorph. Geol. 31, 165–186.
- 95 Gale, M.H., 2007. Bedrock Geologic Map of the Hazens Notch and Portions of the Eden and  
96 Lowell Quadrangles, Vermont. Vt. Geol. Surv., Vermont geological open file report  
97 VG07-2, plate 1.
- 98 Guillot, S., Schwartz, S., Reynard, B., Agard, P., Prigent, C., 2015. Tectonic significance of  
99 serpentinites. Tectonophysics 646, 1–19.
- 100 Hibbard, J.P., Van Staal, C.R., Rankin, D.W., Williams, H., 2006. Lithotectonic map of the  
101 Appalachian orogen, Canada–United States of America. Geol. Surv. Can. Map A 2096,  
102 2.

103 Honsberger, I.W., 2015. Metamorphism, deformation, geochemistry, and tectonics of  
104 exhumed ultramafic and mafic rocks in the central and north-central Vermont  
105 Appalachians.

106 Iyer, K., Austrheim, H., John, T., Jamtveit, B., 2008. Serpentinization of the oceanic  
107 lithosphere and some geochemical consequences: constraints from the Leka  
108 Ophiolite Complex, Norway. *Chem. Geol.* 249, 66–90.

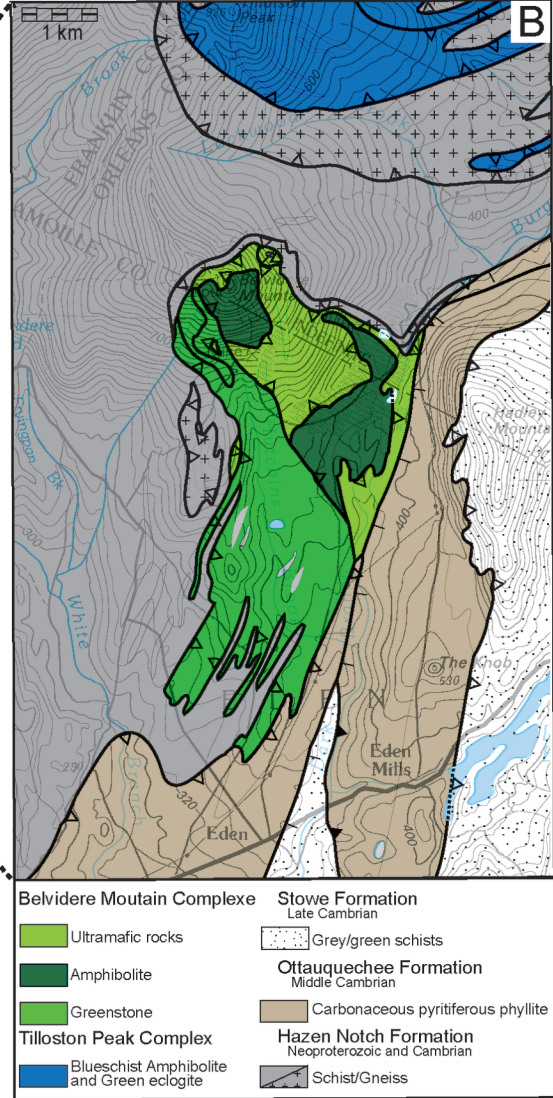
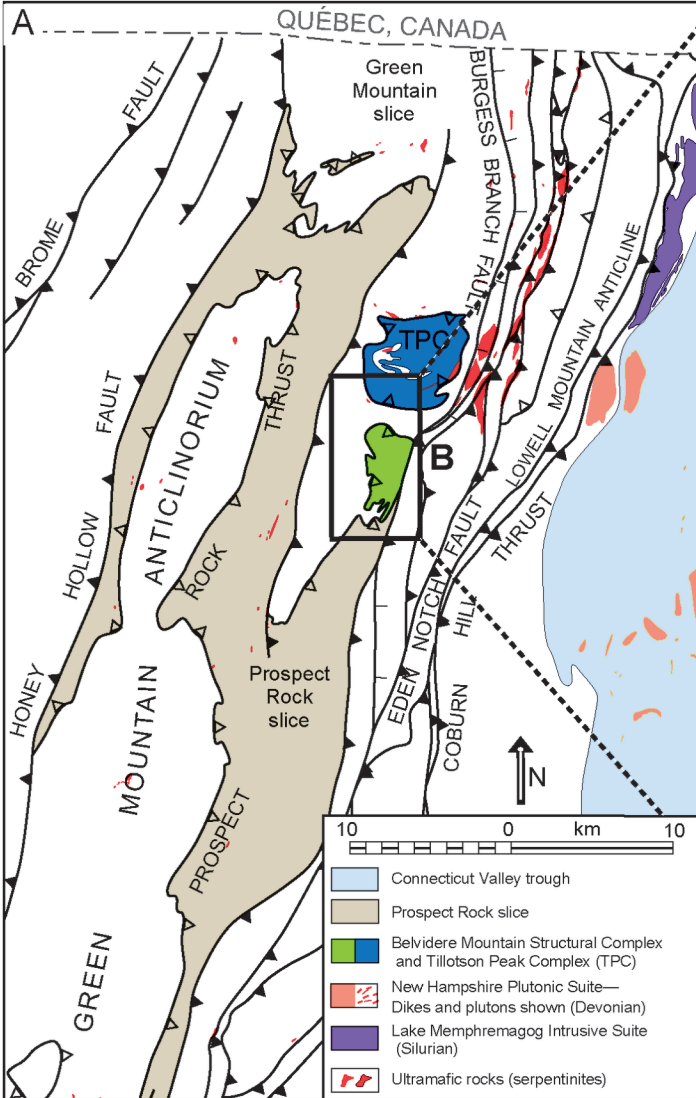
109 Nozaka, T., 2018. Compositional variation of olivine related to high-temperature  
110 serpentinization of peridotites: Evidence from the Oeyama ophiolite. *J. Mineral.  
111 Petrol. Sci.* 180420.

112 Plümper, O., Piazzolo, S., Austrheim, H., 2012. Olivine pseudomorphs after serpentinized  
113 orthopyroxene record transient oceanic lithospheric mantle dehydration (Leka  
114 Ophiolite Complex, Norway). *J. Petrol.* 53, 1943–1968.

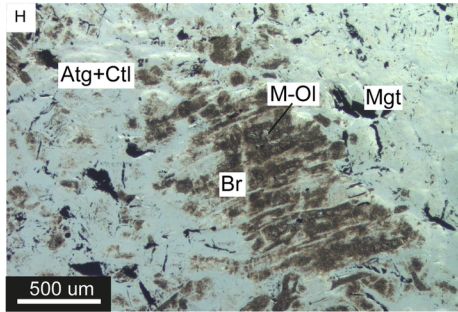
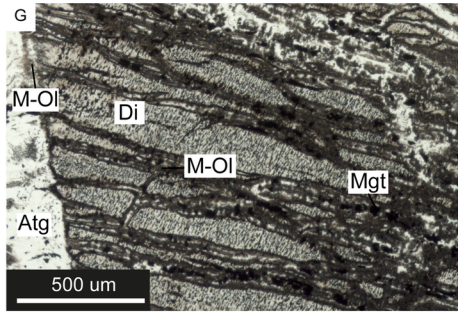
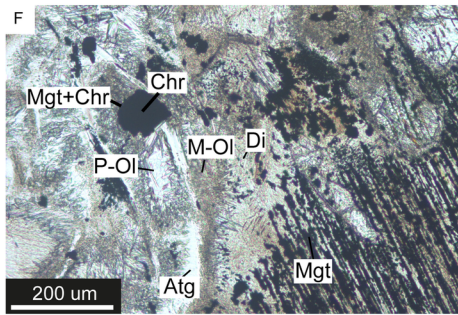
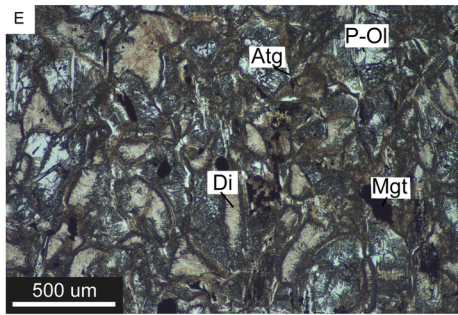
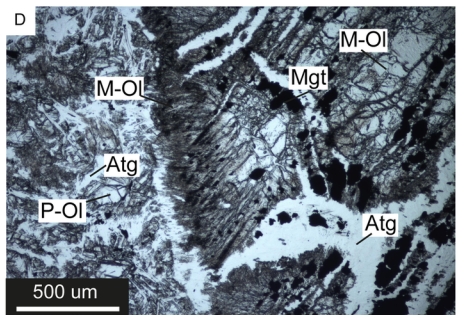
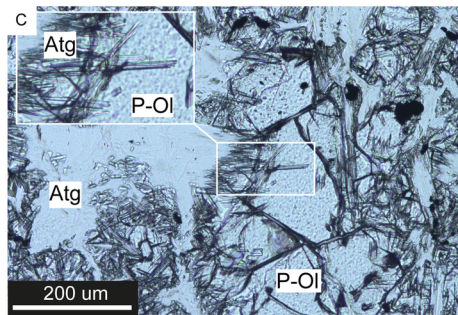
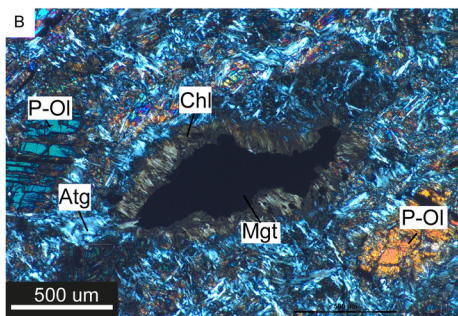
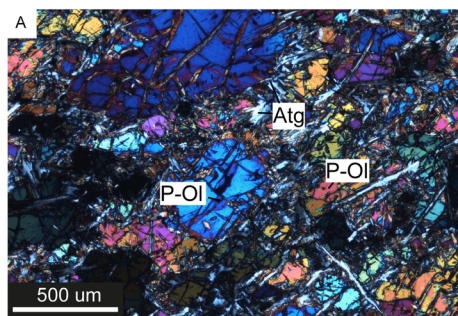
115 Scambelluri, M., Müntener, O., Hermann, J., Piccardo, G.B., Trommsdorff, V., 1995.  
116 Subduction of water into the mantle: history of an Alpine peridotite. *Geology* 23,  
117 459–462.

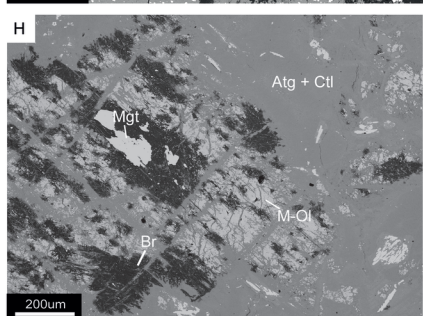
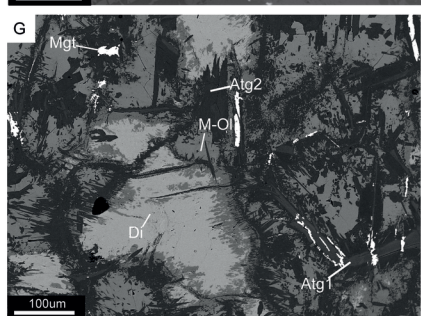
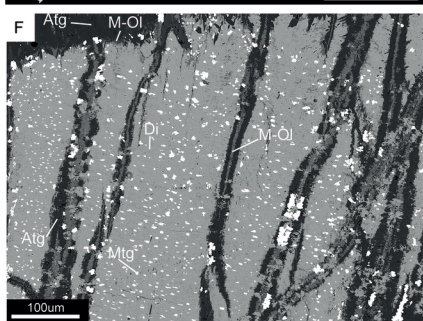
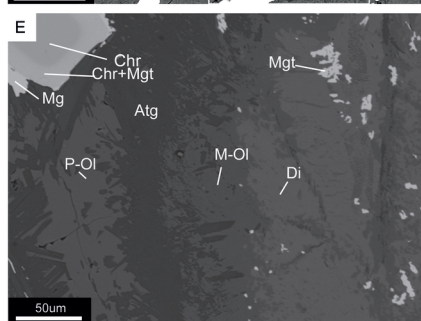
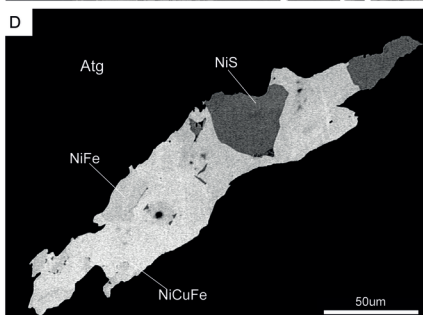
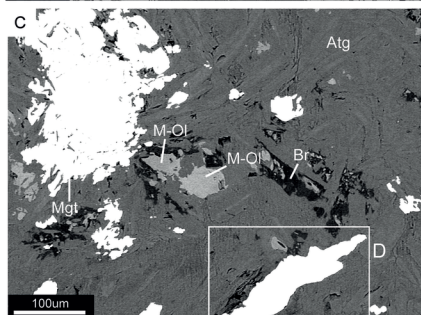
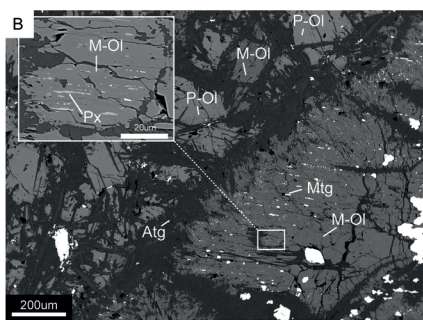
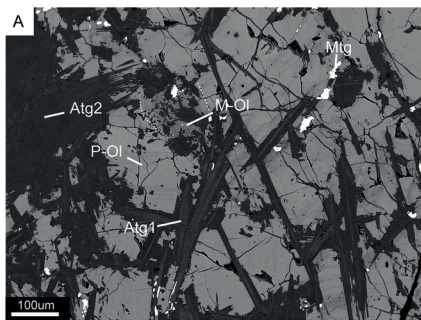
118 Shen, T., Hermann, J., Zhang, L., Lü, Z., Padrón-Navarta, J.A., Xia, B., Bader, T., 2015. UHP  
119 metamorphism documented in Ti-chondrodite- and Ti-clinohumite-bearing  
120 serpentinized ultramafic rocks from Chinese southwestern Tianshan. *J. Petrol.* 56,  
121 1425–1458.

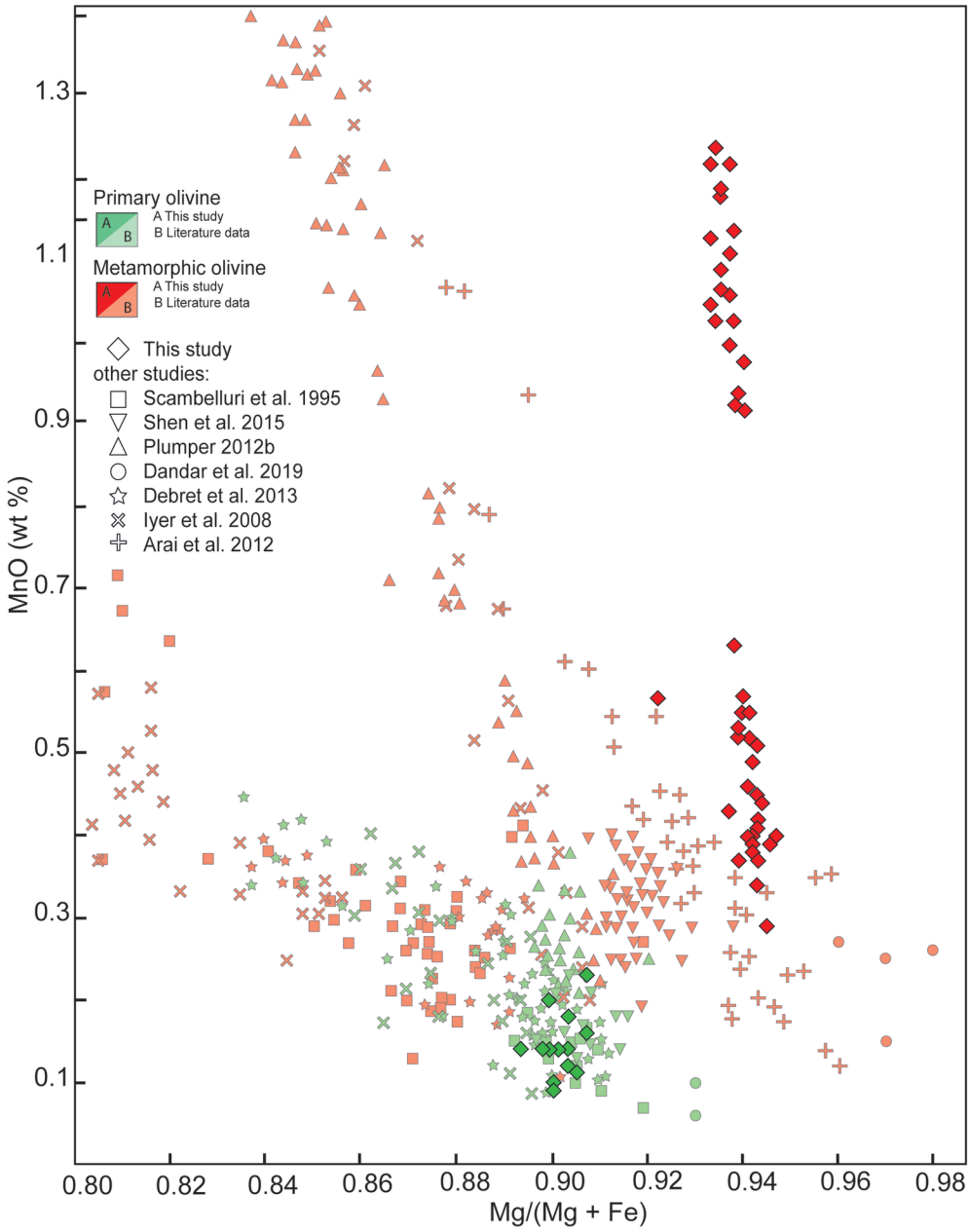
122

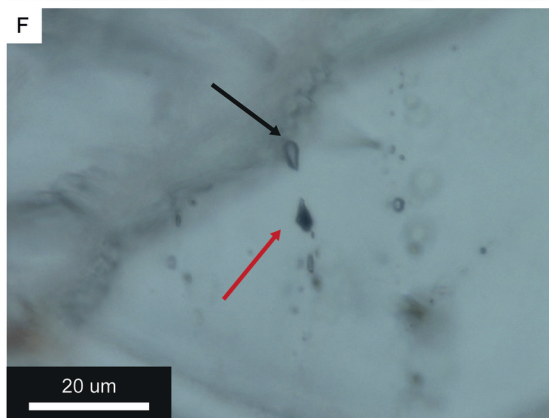
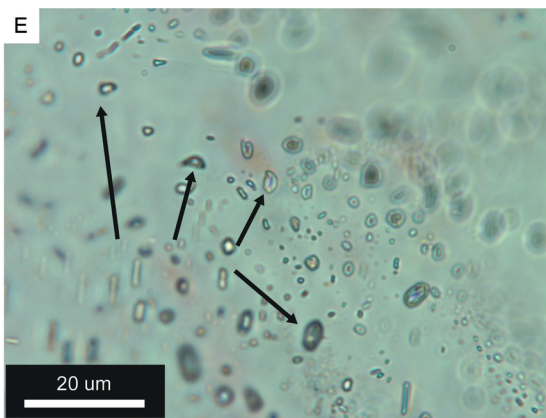
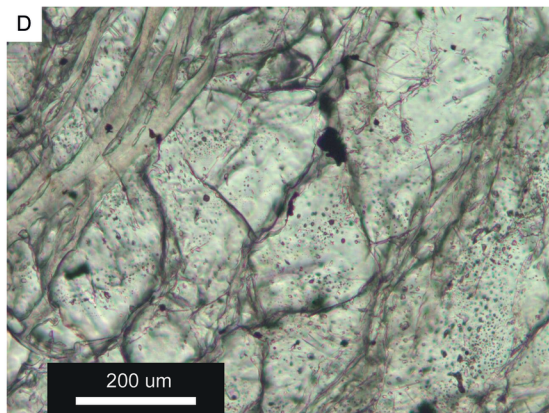
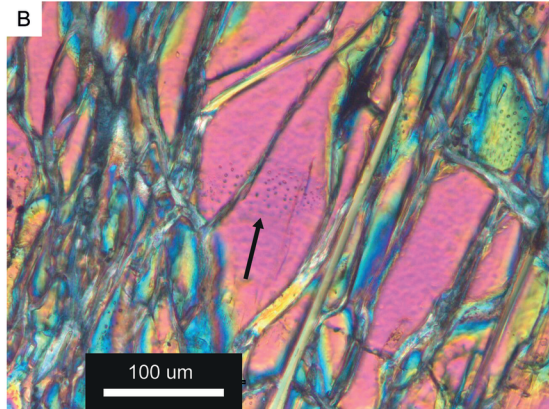
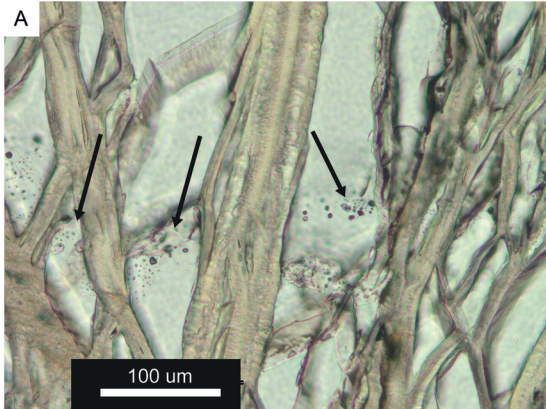


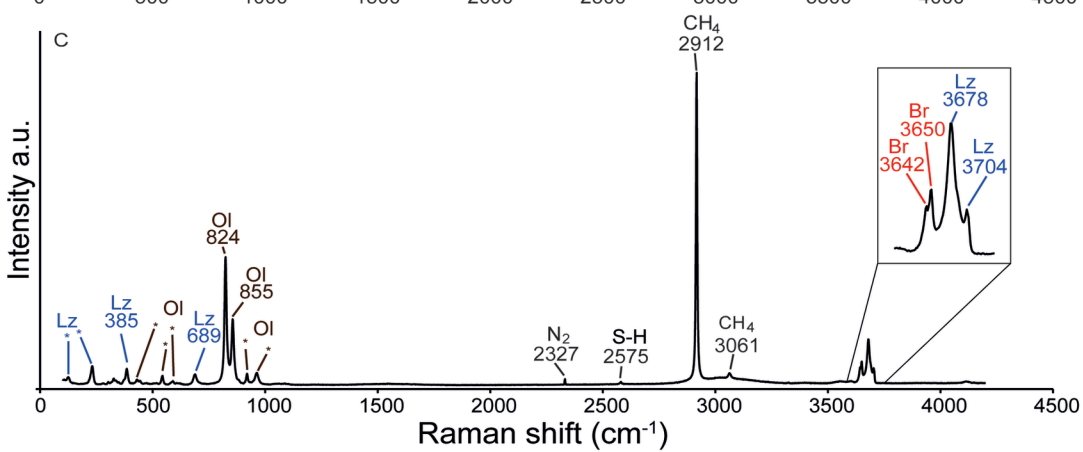
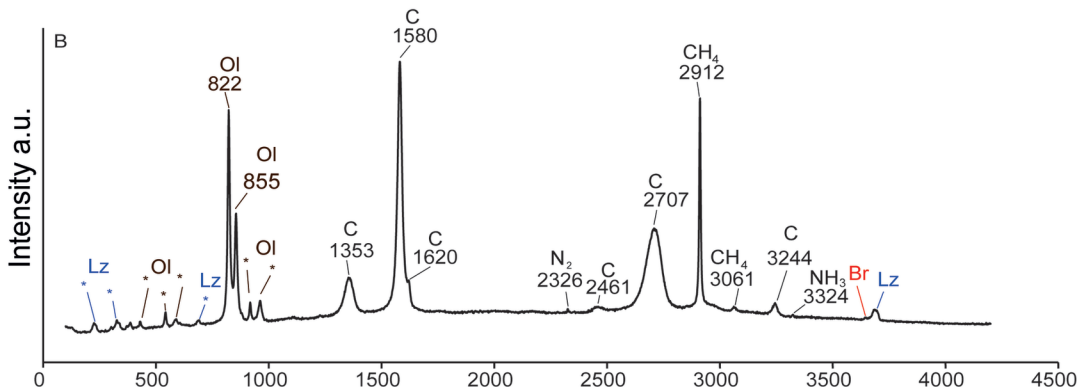
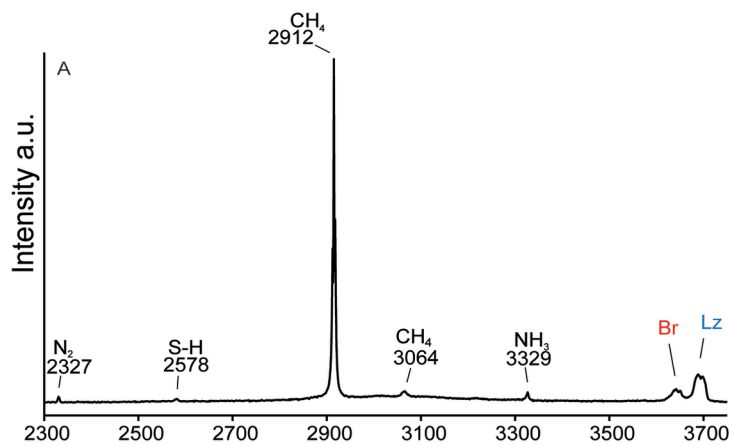


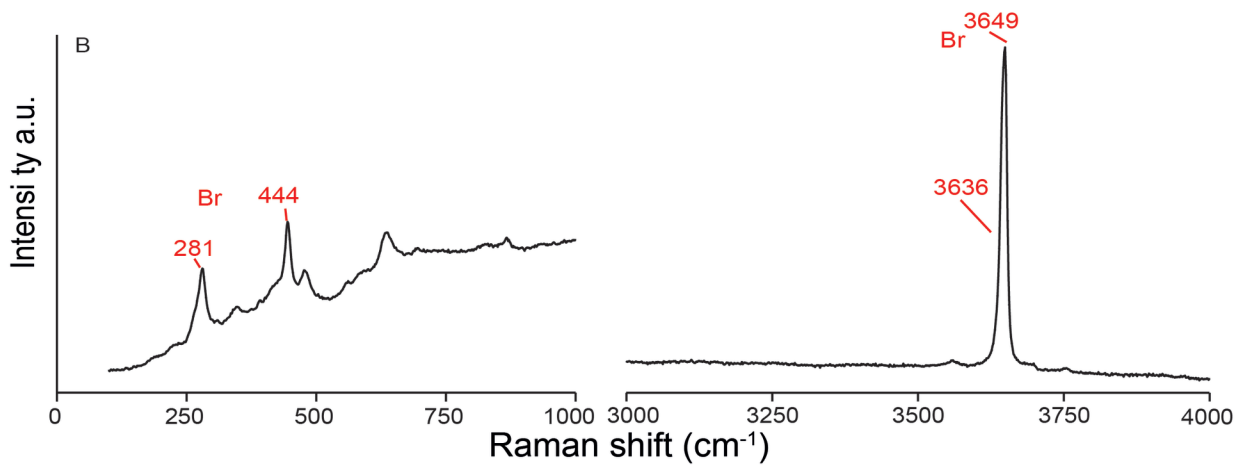
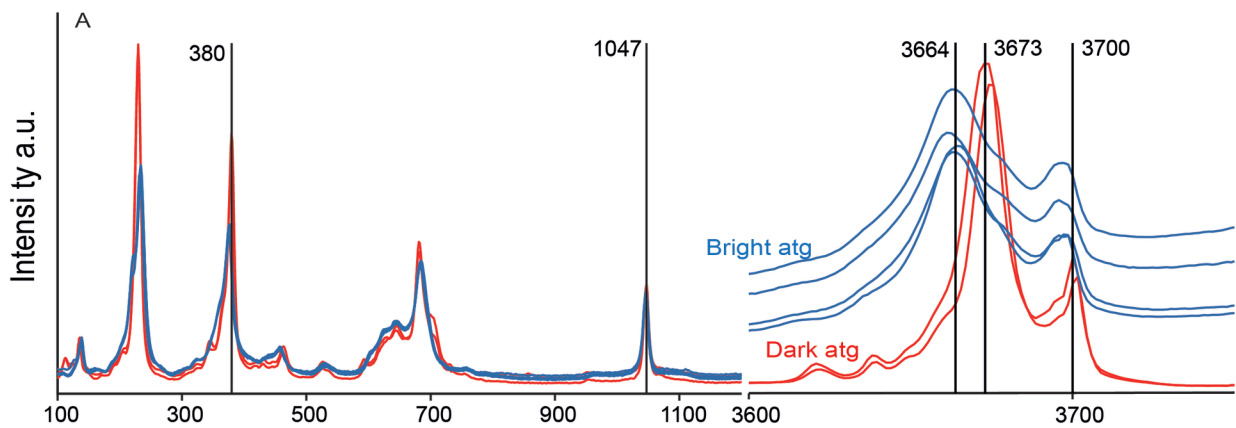


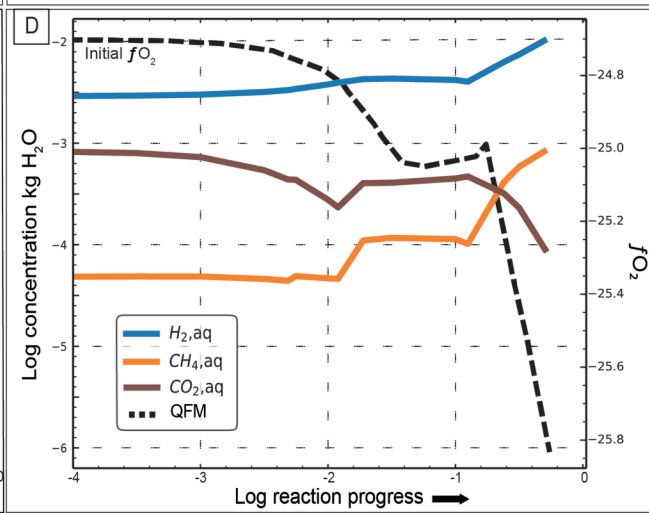
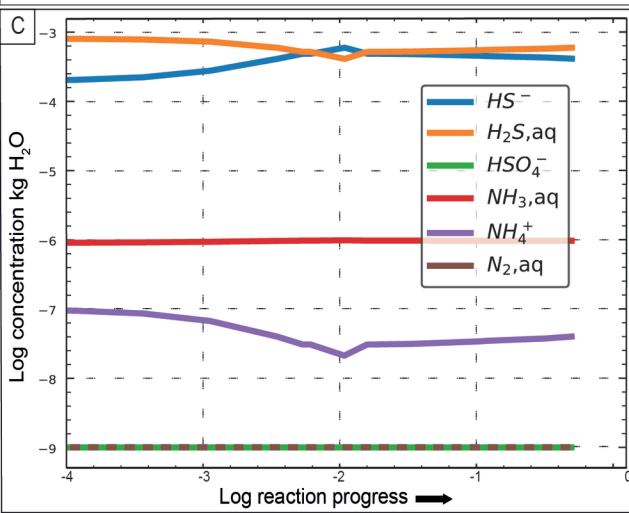
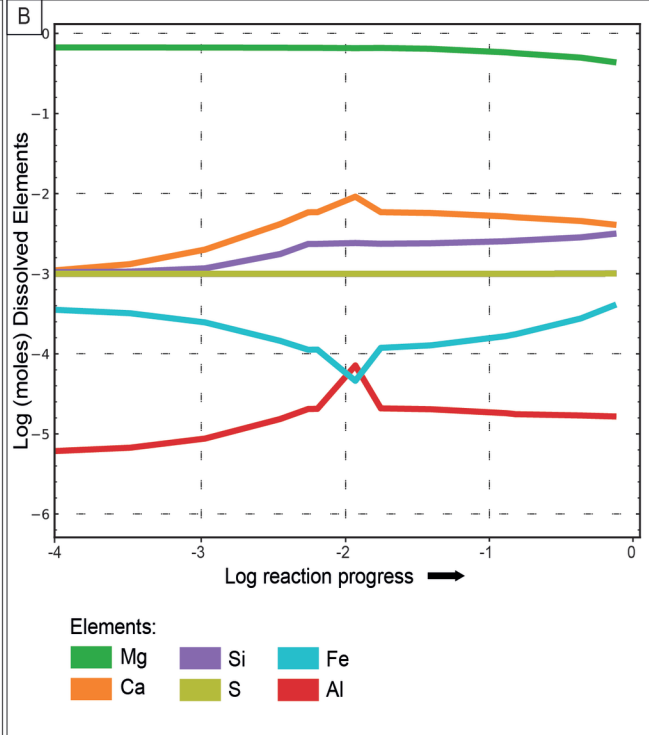
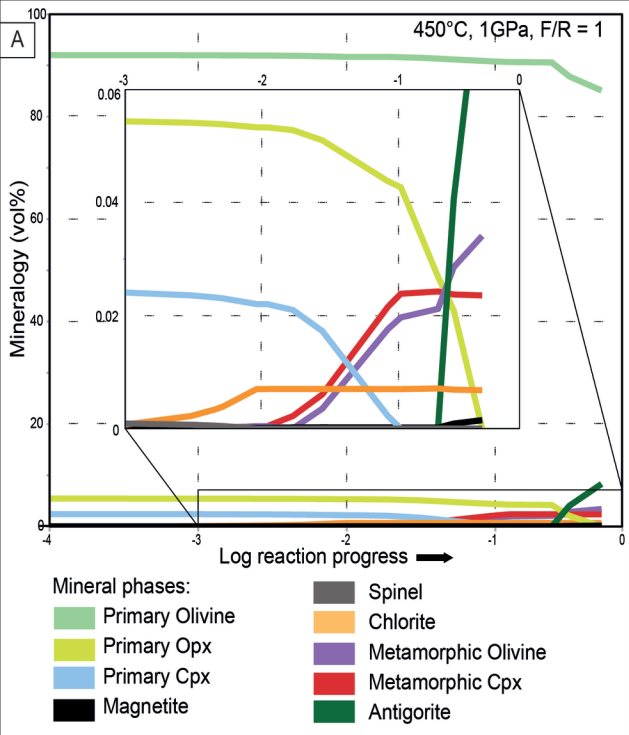




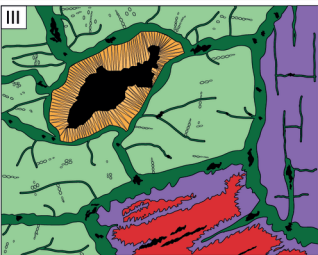
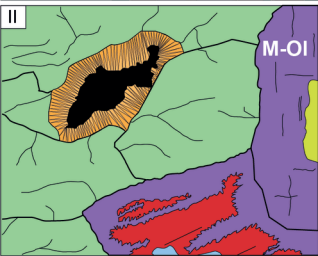
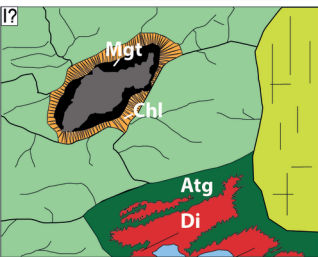
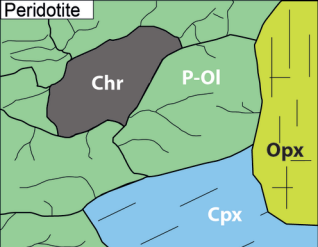






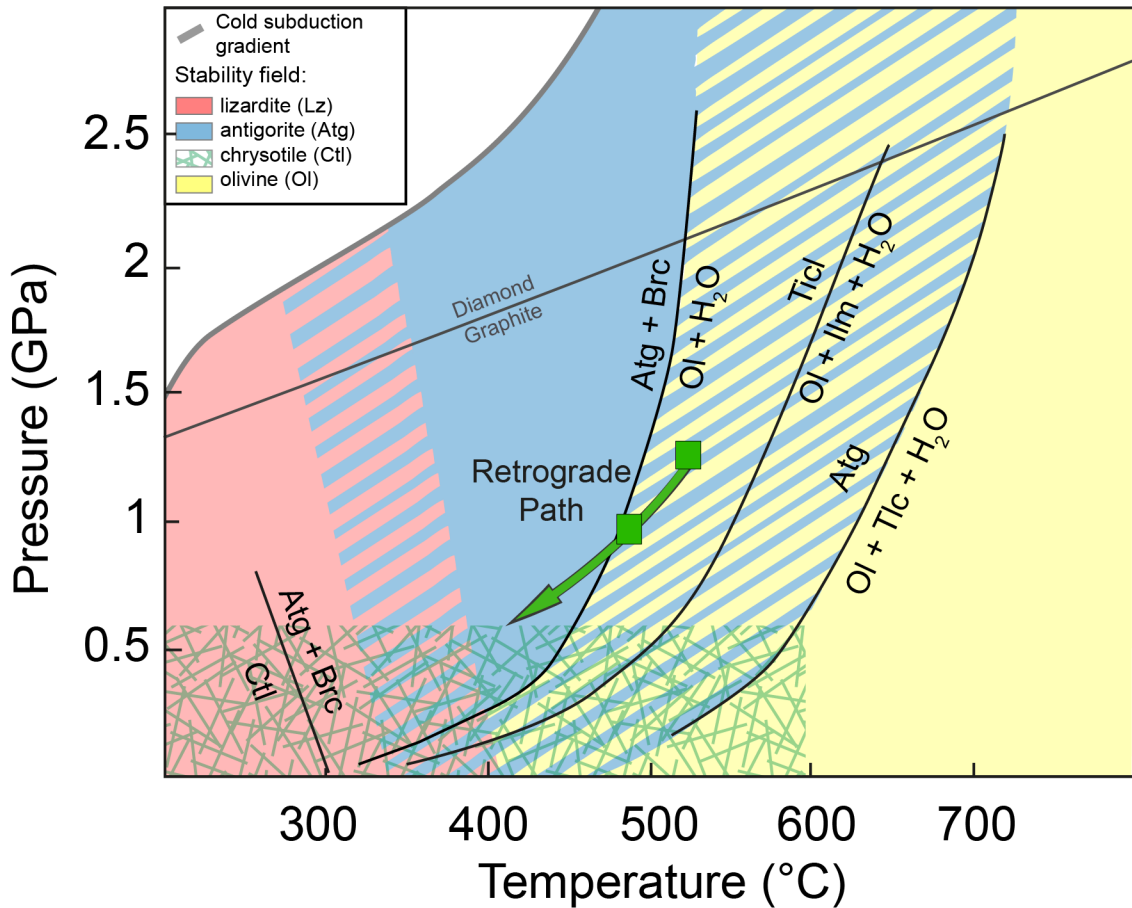


Peridotite



Prograde

Retrograde



1 **Table 1**

MicroProbe analysis. Absence of SD value when n>1 indicates SD<0.01. \*EDS analyses normalized at 100.

Minerals Sample (n)	Primary Olivine		Metamorphic Olivine			Pyroxene	Serpentine (Bright core)		Serpentine (Matrix)		Chlorite	
	V18-2b	V18-3a	V18-2b	V18-3a	V18-B3*	V18-3a	V18-2b	V18-3a	V18-2b	V18-3a	V18-2b	V18-3a
	14	11	28	15	25	20	6	2	9	4	11	1
SiO <sub>2</sub>	40.91 (0.25)	40.83 (0.46)	41.31 (0.49)	41.95 (0.63)	42.00 (0.12)	54.96 (0.98)	42.87 (1.21)	43.41 (0.1)	44.15 (0.17)	43.1 (1.35)	32.61 (1.34)	32.03
TiO <sub>2</sub>	0.01 (0.01)	0.02 (0.02)	0.02 (0.01)	0.02 (0.02)		0.03 (0.02)	0.01 (0.01)	0.02 (0.01)	0.02 (0.01)	0 (0)	0.02 (0.02)	0.00
Al <sub>2</sub> O <sub>3</sub>	0.01 (0.01)	0.01 (0.01)	0.01 (0.02)	0.04 (0.09)		0.15 (0.11)	1.77 (1.22)	1.45 (0.78)	0.52 (0.21)	0.47 (0.26)	14.34 (2.39)	11.78
Cr <sub>2</sub> O <sub>3</sub>	0.01 (0.02)	0.01 (0.02)	0.06 (0.18)	0.04 (0.03)		0.17 (0.11)	0.61 (0.85)	0.25 (0.19)	0.13 (0.09)	0.1 (0.1)	1.07 (0.56)	4.07
FeO (tot)	8.97 (0.34)	7.93 (0.22)	4.83 (0.30)	5.05 (0.57)	4.71 (0.19)	0.76 (0.16)	2.60 (0.26)	1.58 (0.27)	1.35 (0.22)	1.2 (0.29)	3.31 (0.46)	2.79
MnO	0.15 (0.04)	0.12 (0.06)	0.45 (0.08)	0.37 (0.06)	1.02 (0.18)	0.05 (0.03)	0.04 (0.02)	0.05 (0.05)	0.04 (0.02)	0.02 (0.02)	0.06 (0.10)	0.07
NiO	0.38 (0.03)	0.49 (0.06)	0.43 (0.07)	0.39 (0.06)	0.46 (0.08)	0.03 (0.03)	0.16 (0.02)	0.18 (0.06)	0.15 (0.04)	0.19 (0.02)	0.22 (0.05)	0.24
ZnO	0.04 (0.04)	0.03 (0.04)	0.03 (0.04)	0.03 (0.04)		0.01 (0.02)					0.02 (0.04)	0.00
MgO	50.23 (0.22)	50.91 (0.22)	52.8 (0.64)	51.8 (1.57)	51.80 (0.28)	18.75 (1.15)	37.97 (1.30)	39.81 (0.59)	39.6 (0.77)	40.07 (0.61)	34.34 (1.11)	35.08
CaO	0.02 (0.01)	0.01 (0.02)	0.02 (0.02)	0.25 (0.37)		24.87 (1.43)	0.02 (0.02)	0.05 (0.04)	0.02 (0.02)	0.02 (0.01)	0.02 (0.01)	0.05
Na <sub>2</sub> O	0.09 (0.22)	0.01 (0.01)	0.02 (0.02)	0.01 (0.01)		0.04 (0.02)					0.02 (0.03)	0.03
K <sub>2</sub> O	0.01 (0.02)	0.01 (0.01)	0.01 (0.01)	0.01 (0.01)		0.01 (0.01)					0.02 (0.02)	0.02
<b>Total,</b>	<b>100.82 (0.36)</b>	<b>100.37 (0.70)</b>	<b>100.06 (1.10)</b>	<b>99.96 (1.63)</b>	<b>100</b>	<b>99.83 (1.12)</b>	<b>86.2 (0.63)</b>	<b>86.93 (0.4)</b>	<b>86.07 (0.82)</b>	<b>85.25 (1.66)</b>	<b>86.14 (0.65)</b>	<b>86.17</b>
<b>Cations</b>												
O*	4.0	4.0	4.0	4.0	4.0	6.0	6.8	6.8	6.8	6.8	28.0	28.0
Si	0.990	0.988	0.991	1.012	1.013	1.989	1.984	2.010	2.044	1.995	6.232	6.165
Ti	0.000	0.000	0.000	0.000		0.001	0.000	0.001	0.001	0.000	0.004	0.000
Al	0.000	0.000	0.000	0.001		0.006	0.091	0.079	0.028	0.026	3.229	2.672
Cr	0.000	0.000	0.001	0.001		0.005	0.026	0.009	0.005	0.004	0.162	0.619
Fe <sup>2+</sup> (tot)	0.181	0.161	0.097	0.102	0.095	0.023	0.104	0.061	0.052	0.046	0.529	0.404
Mn	0.003	0.003	0.009	0.008	0.021	0.002	0.001	0.002	0.002	0.001	0.010	0.012
Ni	0.007	0.010	0.008	0.008	0.009	0.001	0.006	0.007	0.006	0.007	0.034	0.037
Zn	0.001	0.001	0.000	0.001		0.000					0.003	0.000
Mg	1.812	1.837	1.891	1.861	1.862	1.012	2.486	2.747	2.733	2.765	9.782	10.063
Ca	0.000	0.000	0.001	0.006		0.964	0.001	0.002	0.001	0.001	0.003	0.011
Na	0.004	0.000	0.001	0.000		0.003					0.007	0.012
K	0.000	0.000	0.000	0.000		0.000					0.005	0.005
Mg#	0.91	0.92	0.95	0.95	0.95	0.98	0.94	0.96	0.97	0.97	0.95	0.96

Mg# = Mg/(Mg+ΣFe)

\*As per normalization

3 **Table 2**

MicroProbe analysis. Absence of SD value when n>1 indicates SD<0.01

<b>Minerals</b>	<b>Spinel (nucleus)</b>	<b>Spinel (intermediate)</b>	<b>Magnetite (rim)</b>	<b>Magnetite (mesh and veins)</b>	<b>Brucite</b>	
<b>Sample</b>	<b>V18-3a</b>	<b>V18-3a</b>	<b>V18-3a</b>	<b>V18-3a</b>	<b>V18-2b</b>	<b>V18-2b</b>
<b>(n)</b>	7	7	7	1	4	10
<b>SiO<sub>2</sub></b>	0.02 (0.02)	0.03 (0.01)	0.06 (0.07)	0.07	0.05 (0.03)	0.78 (2.20)
<b>TiO<sub>2</sub></b>	0.09 (0.02)	0.23 (0.05)	0.03 (0.02)	0.04	0.01 (0.01)	0.01
<b>Al<sub>2</sub>O<sub>3</sub></b>	12.63 (0.94)	3.87 (1.34)	0.00	0.03	0.01 (0.01)	0.01 (0.01)
<b>Cr<sub>2</sub>O<sub>3</sub></b>	47.51 (0.57)	41.6 (1.29)	1.87 (1.16)	0.01	0.02 (0.02)	0.04 (0.05)
<b>FeO</b>	34.12 (1.1)	48.32 (2.02)	91.45 (0.75)	92.44	92.57 (0.28)	2.91 (0.18)
<b>MnO</b>	0.34 (0.04)	0.95 (0.36)	0.16 (0.03)	0.12	0.19 (0.05)	0.22 (0.04)
<b>NiO</b>	0.09 (0.02)	0.27 (0.05)	1.05 (0.1)	1.11	0.82 (0.09)	0.38 (0.09)
<b>ZnO</b>	0.49 (0.08)	0.3 (0.1)	0.04 (0.06)	0.10	0.04 (0.08)	0.01 (0.02)
<b>MgO</b>	5.99 (0.32)	3.37 (0.22)	0.71 (0.09)	0.62	0.82 (0.19)	75.88 (3.93)
<b>CaO</b>	0.01 (0.01)	0.00	0 (0.01)	0.00	0.00	0.02 (0.03)
<b>Na<sub>2</sub>O</b>	0.03 (0.04)	0.02 (0.02)	0.03 (0.03)	0.03	0.02 (0.04)	0.02 (0.02)
<b>K<sub>2</sub>O</b>	0.00	0.01 (0.01)	0 (0.01)	0.01	0.00	0.01 (0.01)
<b>Total</b>	101.4 (0.56)	99.03 (0.6)	95.46 (0.5)	94.63	94.56 (0.45)	80.33 (2.70)
<b>Cations</b>						
<b>O*</b>	4.0	4.0	4.0	4.0	4.0	2
<b>Si</b>	0.00	0.00	0.00	0.00	0.00	0.01
<b>Ti</b>	0.00	0.01	0.00	0.00	0.00	0.00
<b>Al</b>	0.49	0.16	0.00	0.00	0.00	0.00
<b>Cr</b>	1.24	1.17	0.06	0.00	0.00	0.00
<b>Fe<sup>3</sup></b>	0.26	0.66	1.94	1.99	2.00	0.00
<b>Fe<sup>2</sup></b>	0.68	0.78	0.92	0.92	0.92	0.02
<b>Mn</b>	0.01	0.03	0.01	0.00	0.01	0.00
<b>Ni</b>	0.00	0.01	0.03	0.03	0.02	0.00
<b>Zn</b>	0.01	0.01	0.00	0.00	0.00	0.00
<b>Mg</b>	0.29	0.18	0.04	0.03	0.05	0.97
<b>Ca</b>	0.00	0.00	0.00	0.00	0.00	0.00
<b>Na</b>	0.00	0.00	0.00	0.00	0.00	0.00
<b>K</b>	0.00	0.00	0.00	0.00	0.00	0.00
<b>Cr#</b>	0.79(0.01)	0.92(0.2)	1.00			

4 Cr# = Cr/(Al+Cr)

5 \*As per normalization

6 **Table 3**

MicroProbe analysis of alloys

Sample	V18-2b						V18-3a		
	NiFeCu	NiS	NiS	NiS	NiFeCu	NiFeCu	NiS	NiS	NiS
<b>S</b>		24.06	24.25	24.12			24.59	24.52	24.50
<b>Fe</b>	12.21	0.9	0.51	1.35	13.35	20.07	0.84		0.95
<b>Pb</b>				0.13			0.18		
<b>Ni</b>	86.23	72.68	72.71	73.55	86.05	80.03	72.97	72.85	73.30
<b>Cu</b>	1.94				1.75	1.49			
<b>Total:</b>	100.45	97.9	97.59	99.18	101.28	101.71	98.70	97.72	99.04

7